



ALMA Observations of Ly α Blob 1: Multiple Major Mergers and Widely Distributed Interstellar Media

Hideki Umehata^{1,2}, Ian Smail³, Charles C. Steidel⁴, Matthew Hayes⁵, Douglas Scott⁶, A. M. Swinbank³, R. J. Ivison⁷, Toru Nagao⁸, Mariko Kubo⁸, Kouichiro Nakanishi^{9,10}, Yuichi Matsuda^{9,10}, Soh Ikarashi³, Yoichi Tamura¹¹, and J. E. Geach¹²

¹RIKEN Cluster for Pioneering Research, 2-1 Hirosawa, Wako-shi, Saitama 351-0198, Japan; hideki.umehata@riken.jp

²Institute of Astronomy, Graduate School of Science, The University of Tokyo, 2-21-1 Osawa, Mitaka, Tokyo 181-0015, Japan

³Centre for Extragalactic Astronomy, Department of Physics, Durham University, South Road, Durham DH1 3LE, UK

⁴Cahill Center for Astrophysics, California Institute of Technology, MC 249-17, 1200 East California Boulevard, Pasadena, CA 91125, USA

⁵Department of Astronomy, Stockholm University, AlbaNova University Centre, SE-106 91, Stockholm, Sweden

⁶Department of Physics and Astronomy, University of British Columbia, 6224 Agricultural Road, Vancouver, BC V6T 1Z1, Canada

⁷European Southern Observatory, Karl-Schwarzschild-Str. 2, D-85748 Garching, Germany

⁸Research Center for Space and Cosmic Evolution, Ehime University, Bunkyo-cho 2-5, Matsuyama 790-8577, Japan

⁹National Astronomical Observatory of Japan, 2-21-1 Osawa, Mitaka, Tokyo 181-8588, Japan

¹⁰Department of Astronomy, School of Science, The Graduate University for Advanced Studies (SOKENDAI), 2-21-1 Osawa, Mitaka, Tokyo, 181-8588 Japan

¹¹Division of Particle and Astrophysical Science, Graduate School of Science, Nagoya University, Aichi 464-8602, Japan

¹²Centre for Astrophysics Research, University of Hertfordshire, Hatfield, AL10 9AB, UK

Received 2021 April 12; revised 2021 June 22; accepted 2021 July 1; published 2021 September 9

Abstract

We present observations of a giant Ly α blob (LAB) in the SSA22 protocluster at $z = 3.1$, SSA22-LAB1, taken with the Atacama Large Millimeter/submillimeter Array. Dust continuum, along with [C II] 158 μm and CO(4–3) line emission have been detected in LAB1, showing complex morphology and kinematics across a ~ 100 kpc central region. Seven galaxies at $z = 3.0987\text{--}3.1016$ in the surroundings are identified in [C II] and dust continuum emission, with two of them potential companions or tidal structures associated with the most massive galaxies. Spatially resolved [C II] and infrared luminosity ratios for the widely distributed media ($L_{[\text{CII}]} / L_{\text{IR}} \approx 10^{-2}\text{--}10^{-3}$) suggest that the observed extended interstellar media are likely to have originated from star formation activity and the contribution from shocked gas is probably not dominant. LAB1 is found to harbor a total molecular gas mass $M_{\text{mol}} = (8.7 \pm 2.0) \times 10^{10} M_{\odot}$, concentrated in the core region of the Ly α -emitting area. While (primarily obscured) star formation activity in the LAB1 core is one of the most plausible power sources for the Ly α emission, multiple major mergers found in the core may also play a role in making LAB1 exceptionally bright and extended in Ly α as a result of cooling radiation induced by gravitational interactions.

Unified Astronomy Thesaurus concepts: [Interstellar medium \(847\)](#); [Intergalactic medium \(813\)](#); [Starburst galaxies \(1570\)](#); [High-redshift galaxy clusters \(2007\)](#); [Circumgalactic medium \(1879\)](#)

1. Introduction

In recent decades, bright and extended nebulae emitting H I Ly α emission have been identified in the early universe. These nebulae, which have extents of several tens to several hundred (physical) kiloparsecs and Ly α luminosity $L_{\text{Ly}\alpha} \sim 10^{43}\text{--}10^{45}$ erg s $^{-1}$, are called Ly α blobs (LABs; e.g., Francis et al. 1996; Ivison et al. 1998; Keel et al. 1999; Steidel et al. 2000; Matsuda et al. 2004; Dey et al. 2005; Ouchi et al. 2009; Yang et al. 2009; Matsuda et al. 2011; Cantalupo et al. 2014; Hennawi et al. 2015; Cai et al. 2017; Kikuta et al. 2019).

The extended emission suggests the presence of plentiful hydrogen on circumgalactic medium (CGM) scales and provides clues to understanding galaxy formation and evolution. For instance, the relation of LABs to the formation of massive galaxies has been proposed (e.g., Dey et al. 2005; Matsuda et al. 2006) and some works suggest that LABs preferentially reside in protoclusters (e.g., Matsuda et al. 2004; Shibuya et al. 2018). Recently Umehata et al. (2019) discovered Ly α filaments on $\gtrsim 1$ physical Mpc scales in the $z = 3.1$ SSA22 protocluster. The filaments encompass two LABs reported in Matsuda et al. (2004), which demonstrates that LABs may be bright knots within gas filaments that are extended over much larger scales and provide fuel for galaxy growth.

What mechanisms produce the Ly α emission is also a subject of debate. The scenarios proposed so far include gravitational cooling radiation associated with pristine, cool hydrogen gas flow (e.g., Dijkstra & Loeb 2009; Faucher-Giguère et al. 2009), galactic winds from starbursts (Taniguchi & Shioya 2000), and photoionization driven by star-forming galaxies or active galactic nuclei (AGNs), followed by scattering (e.g., Geach et al. 2009; Hayes et al. 2011; Steidel et al. 2011).

The SSA22 protocluster at $z = 3.1$ is known to harbor several LABs and hence provides a unique laboratory (Matsuda et al. 2004). Matsuda et al. (2011) performed a 2.1° panoramic survey to discover 14 LABs with linear extents over 100 kpc. Interestingly, the largest and brightest LAB is one of the first discovered LABs, SSA22-LAB1 located close to the protocluster core (hereafter, LAB1 in this paper, Steidel et al. 2000). LAB1 has an extent of ≈ 200 kpc and a luminosity $L_{\text{Ly}\alpha} = 1.1 \times 10^{44}$ erg s $^{-1}$ (Matsuda et al. 2004), making LAB1 one of the most spectacular LABs known to date. Together with its environment, a remarkable protocluster, LAB1 has been intensively investigated by a number of works (e.g., Chapman et al. 2001, 2004; Bower et al. 2004; Geach et al. 2005, 2009, 2014, 2016; Matsuda et al. 2007; Weijmans et al. 2010; Hayes et al. 2011; Uchimoto et al. 2012;

Tamura et al. 2013; Hine et al. 2016; Kubo et al. 2016; Ao et al. 2017; Umehata et al. 2017a; Herenz et al. 2020; Li et al. 2021).

For a comprehensive understanding of the nature of LABs and their role in galaxy formation and evolution, observations at submillimeter wavelengths are of huge importance. Massive star-forming galaxies are easily enshrouded by dust in an intensely star-forming phase, and often undetectable in the optical-to-near-infrared (e.g., Umehata et al. 2020 and references therein). Furthermore, the molecular/fine-structure lines at these wavelengths provide powerful tools to characterize the nature and conditions of the interstellar medium (ISM) in galaxies. Following a number of attempts since the discovery (e.g., Chapman et al. 2001, 2004; Geach et al. 2005, 2014, 2016; Matsuda et al. 2007; Tamura et al. 2013), the advent of the Atacama Large Millimeter/submillimeter Array (ALMA) allows us to revolutionize our picture of LAB1 in this regard. Geach et al. (2016) identified three dusty star-forming galaxies toward LAB1 with a total star formation rate (SFR) of $\sim 200 M_{\odot} \text{ yr}^{-1}$, although only one of the galaxies had a reliable spectroscopic redshift. They proposed that these galaxies identified by ALMA are the dominant sources that power the Ly α emission.

Recently Umehata et al. (2017a) detected the [C II] 158 μm emission line from one massive, dusty star-forming galaxy in LAB1. [C II] 158 μm (${}^2P_{3/2} \rightarrow {}^2P_{1/2}$) is the dominant coolant of the neutral ISM in galaxies and primarily arises from photodissociation regions (PDRs; e.g., Stacey et al. 1991; Israel et al. 1996). Umehata et al. (2017a) found that the [C II] emission is relatively strong compared to the infrared luminosity and [N II] emission and suggested that these characteristics of the ISM are influenced by the location within the giant LAB. These previous works have gradually uncovered the hidden aspects of LAB1, including the dust-obscured star formation and the nature of the ISM. However, the sensitivity and resolution of the observations were limited.

Here, we present results from newly obtained deep [C II], CO(4–3), and dust continuum observations of LAB1 in conjunction with Ly α observations. In Section 2, we detail the observations and data reduction. In Section 3, we describe the source decomposition and flux measurements of the dust continuum emission. In Section 4, we derive various properties of the [C II] and CO(4–3) emission, including kinematics and counterpart identification. We discuss the ISM nature, the phase of galaxy assembly, and powering sources of the Ly α emission in Section 5, and present our conclusions in Section 6. Throughout the paper, we adopt a cosmology with $\Omega_{\text{m}} = 0.3$, $\Omega_{\Lambda} = 0.7$, and $H_0 = 70 \text{ km s}^{-1} \text{ Mpc}^{-1}$.

2. Observations and Data Reduction

2.1. Overview of ALMA Data

LAB1 has been targeted by several ALMA projects. We utilized observations in ALMA Band 3, Band 7, and Band 8, combining both newly obtained data and archival data. The top left panel of Figure 1 shows a false color map taken with Subaru/Suprime-Cam (Hayashino et al. 2004) and Multi-object Infrared Camera and Spectrograph (MOIRCS) (Uchimoto et al. 2012) with Ly α contours observed by the Multi Unit Spectroscopic Explorer (MUSE; Bacon et al. 2010). Two LABs were individually identified and labeled as LAB1 and LAB8, originally (Steidel et al. 2000; Matsuda et al. 2004). A deeper Ly α map has uncovered that the two LABs are connected to each other (Geach

et al. 2016; Herenz et al. 2020; Li et al. 2021). As shown in Figure 1, observations in ALMA Band 7 and Band 8 cover LAB1 almost entirely, while ALMA Band 3 observations cover both LAB1 and LAB8 within the field of view. In this paper, we focus on LAB1. The details of the ALMA observations and data reductions are as follows.

2.2. ALMA Band 8

The first observations of LAB1 in ALMA Band 8 were carried out in Cycle 2 as reported in Umehata et al. (2017a) (ID: 2013.1.00159.S; PI: H. Umehata). In the pilot survey, the central coordinate was $(\alpha, \delta) = (22^{\text{h}}17^{\text{m}}26.0^{\text{s}}, 0^{\text{h}}12^{\text{m}}37.5^{\text{s}})$ (International Celestial Reference System (ICRS)) and the on-source time was 4.5 minutes. Subsequently we performed deeper imaging in ALMA Cycle 5 (Program ID: 2017.1.01209.S, PI: H. Umehata). We set central coordinates of $(\alpha, \delta) = (22^{\text{h}}17^{\text{m}}25.9^{\text{s}}, 0^{\text{h}}12^{\text{m}}36.3^{\text{s}})$ (ICRS). We note that the pointing was slightly shifted, considering the results of the dust continuum at Band 7 (Geach et al. 2016; Ao et al. 2017) and the results of the pilot [C II] observations, which were available at the time of the preparation.

The observations were carried out between 2018 May and July with 44–45 available 12 m antennas in the C43-1 and C43-2 configurations. The baseline lengths span from 15–313 m. The precipitable water vapor was in the range of 0.2–0.6 mm and the weather conditions were excellent or acceptable for Band 8 observations. The exposure time totaled 116.5 minutes after combining Cycle 2 and Cycle 5 observations. We used the Frequency Division Modes (FDM) correlator and set the central frequencies of four spectral windows as 451.51, 453.09, 463.14, and 464.77 GHz. Each spectral window had 1920 channels and the resultant channel width was approximately 1 MHz. The quasars J2253+1608 and J2258-2758 were observed for bandpass and flux calibration and the quasar J2226+0052 was utilized for phase calibration.

Each measurement set was calibrated using the Common Astronomy Software Application (CASA) v5.1.1 (McMullin et al. 2007), utilizing the standard reduction pipeline. Imaging the uv data was performed using CASA v5.6.1. We first Fourier transformed the uv data to obtain a dirty cube using the TCLEAN task, adopting natural weighting. We then analyzed the cube to extract the [C II] emission. For this, we focused on two of the four spectral windows, which cover a frequency range of 462.16–465.62 GHz contiguously, corresponding to frequencies of [C II] at $z \simeq 3.1$. We measured the rms level for each channel in a line-free region and cleaned to 2σ , placing masks for the [C II]-emitting regions. Imaging with natural weighting yields a typical synthesized beam of $0.75'' \times 0.63''$ (P.A. = -80°). This cube is called the 0.8'' cube in this paper. We applied the IMCONTSUB task to subtract continuum emission in the image plane. The resultant rms level at the phase center is $0.50 \text{ mJy beam}^{-1}$ with a 20 km s^{-1} velocity bin, while some frequency ranges have relatively higher rms levels, affected by lower atmospheric transmission in Band 8. The primary beam response was corrected. To extract spatially extended emission and also perform an angular-resolution-matched comparison with CO(4–3) and $860 \mu\text{m}$ data, we also produce $1.0''$ and $1.4''$ cubes in the same way but applying varying uv tapering and 80 km s^{-1} velocity bins. The two cubes have synthesized beams and typical rms levels of $0.97'' \times 0.84''$ (P.A. = -83°) and $0.30 \text{ mJy beam}^{-1}$, and $1.44'' \times 1.32''$ (P.A. = -87°) and $0.39 \text{ mJy beam}^{-1}$, respectively.

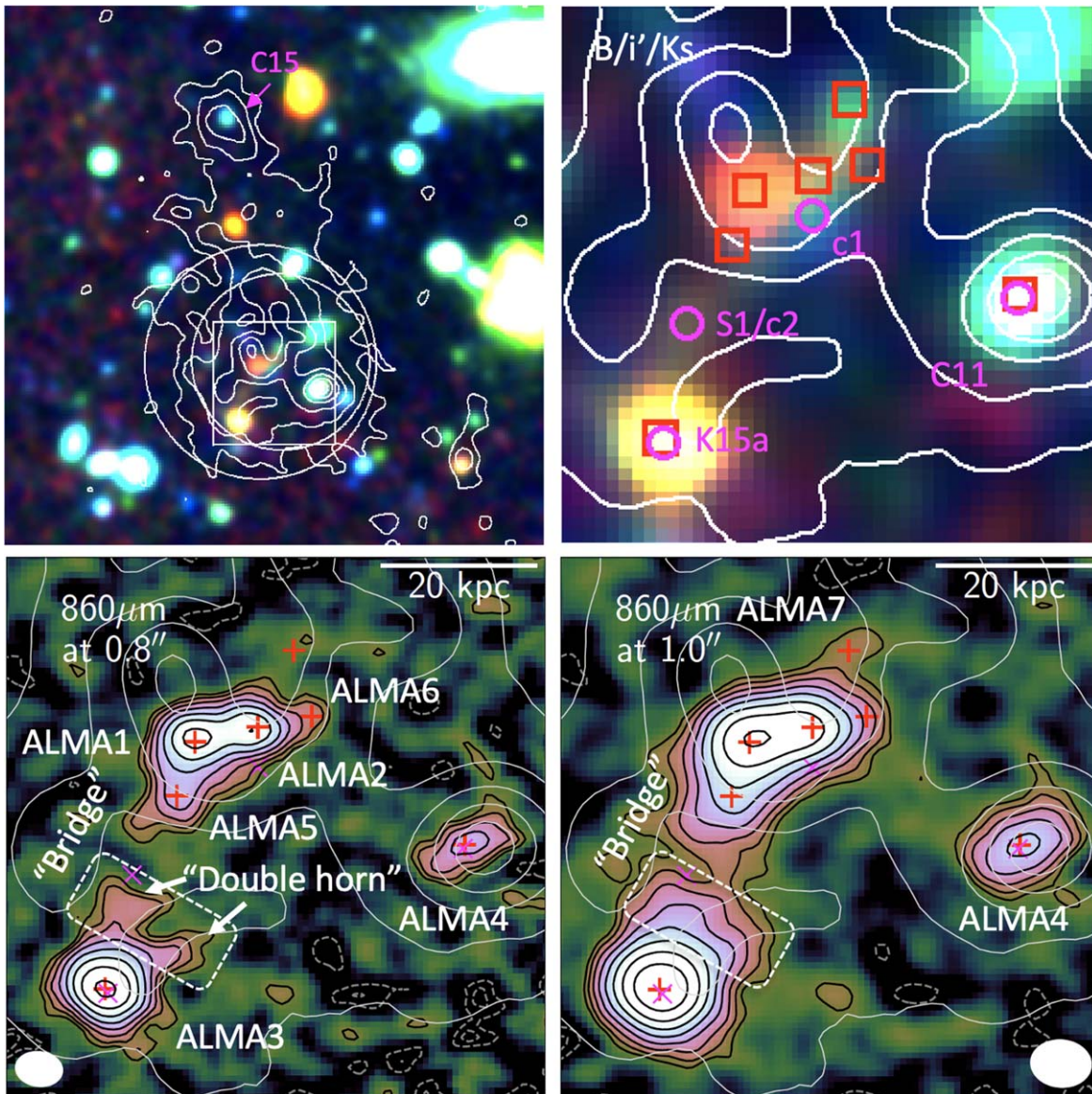


Figure 1. The left panel shows a false color map of LAB1 (Subaru/Suprime-Cam B band (blue), Subaru/Suprime-Cam, i' band (green); Subaru/MOIRCS K_s band (red), Hayashino et al. 2004). White contours show $\text{Ly}\alpha$ surface brightness of $\mu = [5, 14, 26, 40, 56, 73] \times 10^{-19} \text{ erg s}^{-1} \text{ cm}^{-2} \text{ arcsec}^{-2} \text{ \AA}^{-1}$ averaged over 4969–5004 \AA . ALMA fields of view are also shown by the two circles (small: Band 7, 8, large: Band 3). A zoomed $9'' \times 9''$ region (white box in the top left) is shown in a top right panel. The bottom two panels show $860 \mu\text{m}$ continuum images of the same field. Thick contours show $[\pm 1.5^2, \pm 1.5^3, \dots] \times \sigma_{\text{center}}$, where σ_{center} is the rms level at the phase center in each map. ALMA sources (red boxes or crosses) and other known $z \approx 3.1$ galaxies with [O III] 5008 line detections are labeled (magenta circles or crosses). The $860 \mu\text{m}$ images reveal widely extended dust components.

A continuum image was also created in the same way, using line-free channels in all spectral windows. The map has a representative frequency of 458.097 GHz and a synthesized-beam of $0.75'' \times 0.63''$ (P.A. = -81°). The 1σ sensitivity at the phase center is $52 \mu\text{Jy beam}^{-1}$.

2.3. ALMA Band 7

Following the first two observations in ALMA Cycle 2 (Program ID: 2013.1.00704.S, PI: Y. Matsuda, Program ID: 2013.1.00922.S, Geach et al. 2016; Ao et al. 2017), LAB1 was further observed in ALMA Band 7 by two projects. In ALMA Cycle 4 (Program ID: 2016.1.01134.S, PI: J. Geach), observations were performed to obtain a deeper continuum map at $850 \mu\text{m}$, centered at $(\alpha, \delta) = (22^{\text{h}}17^{\text{m}}26.0^{\text{s}}, 0^{\text{h}}12^{\text{m}}34.7^{\text{s}})$ (ICRS). The observations were carried out on 2017 April 4

and 5, using 38–39 usable 12 m antennas under good weather conditions. The C40-1 array configuration utilized was the most compact configuration at the time (baseline lengths of 15–279 m), which was suitable to detect extended components. The representative frequency was 354.60 GHz and the total on-source time was 82 minutes. The quasars, J2148+0657 and J2232+1143 were observed for calibration. Each measurement set was calibrated in CASA v4.7.2, utilizing the standard reduction pipeline.

LAB1 was also observed in ALMA Band 7 as a part of the Cycle 5 project (Program ID: 2017.1.01209.S, PI: H. Umehata) to detect dust continuum and [N II] $205 \mu\text{m}$ emission. We will report the result of [N II] $205 \mu\text{m}$ emission in a separate paper (H. Umehata et al., in preparation). Observations were carried out on 2018 May 30 and 31, using 45–46 available 12 m antennas, under good weather conditions. The C43-2 array

Table 1
Continuum Properties of ALMA Sources in LAB1

Source	R.A. [h m s]	Decl. [$^{\circ}$ ' '']	$S_{656\mu\text{m}}^{0.8}$ [mJy]	$S_{860\mu\text{m}}^{0.8}$ [mJy]	$S_{860\mu\text{m}}^{1.0}$ [mJy]	$S_{2.82\text{mm}}^{1.4}$ [mJy]	Other ID
ALMA1	22 17 26.01	+00 12 36.4	$1.56 \pm 0.20^{\text{a}}$	0.50 ± 0.02	0.51 ± 0.01	<0.010	ALMA-a (1), K15c (2)
ALMA2	22 17 25.94	+00 12 36.7	0.70 ± 0.15	0.38 ± 0.02	$0.48 \pm 0.01^{\text{a}}$...	ALMA-b (1)
ALMA3	22 17 26.11	+00 12 32.3	2.49 ± 0.31	0.86 ± 0.02	0.97 ± 0.01	0.022 ± 0.006	ALMA-c (2), K15a (2)
ALMA4	22 17 25.71	+00 12 34.7	0.56 ± 0.16	0.20 ± 0.01	0.23 ± 0.005	<0.010	C11 (3)
ALMA5	22 17 26.03	+00 12 35.5	<0.17 ^a	0.17 ± 0.01	0.17 ± 0.01	... ^b	...
ALMA6	22 17 25.88	+00 12 36.9	<0.16	0.05 ± 0.005	$0.03 \pm 0.002^{\text{a}}$... ^b	...
ALMA7	22 17 25.90	+00 12 38.0	<0.16	<0.04	0.06 ± 0.006	... ^b	...
Bridge	0.20 ± 0.05

Notes. References are denoted as follows: (1) Geach et al. (2016), (2) Kubo et al. (2016), and (3) Steidel et al. (1998).

^a Some fraction of fluxes of fainter sources may be underestimated due to difficulty of source deblending.

^b Upper limits are shown only for the brightest three sources since the beam size is too large to isolate limits on fainter sources.

configuration was used, which resulted in a range of baselines of 15–314 m. The central position was $(\alpha, \delta) = (22^{\text{h}}17^{\text{m}}26.0^{\text{s}}, 0^{\text{h}}12^{\text{m}}37.1^{\text{s}})$ (ICRS). The total on-source time was 2.4 hr, which was divided into three execution blocks. The TDM correlator was utilized to have a representative frequency of 356.3735 GHz. The two sidebands have a frequency gap of 8 GHz between them, and each sideband has two spectral windows with 1.875 GHz bandwidth and 31.25 MHz resolution. The nearby quasar J2226+0052 was observed regularly to calibrate amplitude and phase, while J2253+1608 was observed for bandpass, pointing, and absolute flux calibration. Each measurement set was calibrated in CASA v5.1.1, utilizing the standard reduction pipeline.

All available Band 7 data were mapped using the TCLEAN task in CASA. As for Band 8, maps with three angular resolutions were created. We excluded channels which cover the redshifted [N II] 205 μm emission in the continuum imaging. We then cleaned to 2σ , masking bright sources. The resulting image has a representative frequency of 347.565 GHz. Imaging with the Briggs parameter 0.5 resulted in the synthesized beam $0.79'' \times 0.59''$ (P.A. = 83°) and we refer to it the “0.8” image”. Images obtained using natural weighting provide images with the synthesized beam $1.02'' \times 0.80''$ (P.A. = -81°) and $1.54'' \times 1.34''$ (P.A. = -81°) without and with tapering, respectively. We refer to these as the 1.0” and 1.4” images. The 1σ sensitivity is 11, 12, and 16 $\mu\text{Jy beam}^{-1}$ at the phase center, for the 0.8”, 1.0”, and 1.4” images, respectively.

2.4. ALMA Band 3

LAB1 was observed in ALMA Band 3 in its Cycle 4 (Program ID: 2016.1.00485.S, PI: N. Hine). The central position was $(\alpha, \delta) = (22^{\text{h}}17^{\text{m}}26.0^{\text{s}}, 0^{\text{h}}12^{\text{m}}37.6^{\text{s}})$ (ICRS). Observations were carried out in 2016 December with 41–46 usable 12 m antennas. The baseline lengths ranged from 15–243 m. The total on-source time was 4.6 hr, divided into six individual execution blocks (EBs). The quasars J2148+0657 and J2226+0052 were observed for pointing, amplitude, bandpass, and phase calibration. The absolute flux scale was set using observation of Neptune. Each measurement set was calibrated in CASA v4.7.0, utilizing the standard reduction pipeline. Data were mapped using the TCLEAN task in CASA with natural weighting. Our primary target was the CO(4–3) line at $z \sim 3.1$, and a cube was created and cleaned to 2σ with bright sources masked. The resultant size of the synthesized

beam is $1.53'' \times 1.30''$ (P.A. = -33°) at 112.52 GHz. The typical rms level at the phase center is $0.70 \mu\text{Jy beam}^{-1}$ with 80 km s^{-1} velocity bins. We also made a continuum map from line-free channels using TCLEAN. The map has a synthesized beam of $1.61'' \times 1.39''$ (P.A. = -33°) and 1σ sensitivity of 4.9 μJy at 106.28 GHz.

2.5. MUSE

LAB1 has been observed by MUSE on UT4 of the Very Large Telescope in three programs (094.A-0605 PI: M. Hayes, 095.A-0570 PI: R. Bower, and 097.A-0831 PI: M. Hayes), which provides a three-dimensional data cube containing Ly α emission (Geach et al. 2016; Herenz et al. 2020). The typical individual exposure times are 1500 s and the total on-source time is 17.6 hr. Seeing was typically about 1” (see Herenz et al. 2020 for details). Data were reduced with the MUSE pipeline (Weilbacher et al. 2016), following standard procedures. Flat fielding and sky subtraction were performed with an additional correction to homogenize the illumination across the field (e.g., Swinbank et al. 2017; Umehata et al. 2019). The resultant cube has wavelength bins of 1.25 Å. In this work, all wavelengths were finally specified in vacuum with AIRTOVAC in the MPDAF package (Bacon et al. 2016; Piqueras et al. 2017) using the relation of Ciddor (1996). We use the vacuum wavelength 1215.67 Å for Ly α .

3. Dust Continuum in LAB1

Continuum maps of LAB1 at 860 μm are shown in Figure 1, compared with the Ly α emission. As shown, the newly obtained ALMA continuum maps in Band 7 have changed our view of this system; multiple cold dust emission components are discovered across LAB1, including three galaxies previously identified by Geach et al. (2016).

To isolate the emission from each component, bright sources were sequentially modeled and subtracted using CASA/IMFIT. This results in identification of seven dusty galaxies, ALMA1–ALMA7 as labeled in Figure 10 (see Figure 9 for model and residual images). Geach et al. (2016) suggested the existence of a *tail* connected to ALMA1, lying to the south. This may be associated with ALMA5, although the low signal-to-noise ratio of the image presented in Geach et al. (2016) precludes a definitive conclusion. There is an additional dusty component located between ALMA3 and ALMA5. This *Bridge* region shows a double horn shape (Figure 1).

Table 2
ISM Properties of Components in LAB1 at 1.4'' Resolution

		ALMA1+ALMA2+ALMA5	ALMA3	ALMA4
CO(4–3)	Coordinates (ICRS)	22:17:26.00+00:12:36.1	22:17:26.10+00:12:32.2	...
	$z_{\text{CO(4-3)}}$	3.0982 ± 0.0002	3.0989 ± 0.0004	...
	Diameter ^a [kpc]	$(12.7 \pm 1.8) \times (7.5 \pm 1.5)$	Point source	...
	FWHM [km s ⁻¹]	322 ± 29	316 ± 65	...
	$S\Delta v$ [Jy km s ⁻¹]	0.44 ± 0.03	0.12 ± 0.02	$<0.03^b$
	$L_{\text{CO(4-3)}} [10^7 L_{\odot}]$	3.6 ± 0.3	1.0 ± 0.2	<0.3
	$M_{\text{gas}}^{\text{CO(4-3)}} [10^{10} M_{\odot}]^c$	6.8 ± 1.5	1.7 ± 0.5	<0.5
[C II]	Coordinates (ICRS)	22:17:26.00+00:12:36.0	22:17:26.11+00:12:32.3	22:17:25.71+00:12:34.6
	$z_{\text{[CII]}}$	3.0983 ± 0.0002	3.0993 ± 0.0001	3.0985 ± 0.0001
	Diameter ^a [kpc]	$(17.2 \pm 2.9) \times (7.3 \pm 2.5)$	$(8.5 \pm 1.0) \times (4.6 \pm 1.5)$	point source
	FWHM [km s ⁻¹]	370 ± 30	337 ± 11	193 ± 24
	$S\Delta v$ [Jy km s ⁻¹]	8.12 ± 0.57	13.20 ± 0.38	1.65 ± 0.18
	$L_{\text{[CII]}} [10^8 L_{\odot}]$	27.3 ± 1.9	44.4 ± 1.3	5.6 ± 0.6
860 μm	Coordinates (ICRS)	22:17:25.99+00:12:36.4	22:17:26.10+00:12:32.4	22:17:25.71+00:12:34.7
	Diameter ^a [kpc]	$(15.0 \pm 1.4) \times (6.5 \pm 1.2)$	$(8.9 \pm 1.3) \times (6.6 \pm 1.8)$	$(6.9 \pm 0.8) \times (3.1 \pm 2.3)$
	S_{860} [mJy]	1.27 ± 0.09	1.17 ± 0.07	0.22 ± 0.01
	$M_{\text{dust}}^{860} [10^8 M_{\odot}]^d$	≈ 2.0	≈ 1.9	≈ 0.4
	$L_{\text{IR}[8-1000]} [10^{12} L_{\odot}]^e$	1.05 ± 0.34	0.97 ± 0.31	0.18 ± 0.06
	$\text{SFR}_{\text{IR}} [M_{\odot} \text{ yr}^{-1}]^e$	110 ± 40	100 ± 30	20 ± 6

Notes. CO and [C II] spectra are extracted using apertures shown in Figure 2 (Figure 3). Properties are generally derived via fits with a single Gaussian profile on the spectra, while the CASA/IMFIT task is also utilized to derive coordinates and sizes. For the 860 μm data, CASA/IMFIT are utilized to derive properties.

^a Deconvolved major and minor axes of FWHM measured by CASA/IMFIT are presented.

^b 3σ point source limit with an assumption of a velocity width (320 km s⁻¹).

^c Brightness temperature ratio $r_{41} = 0.61 \pm 0.13$ (Boogaard et al. 2020) and a CO-to-H₂ conversion factor $\alpha_{\text{CO}} = 3.6$ (as in Decarli et al. 2020) are assumed.

^d M_d values are calculated assuming modified blackbody radiation with $\beta = 1.8$ and $T_d = 40$ K.

^e L_{IR} and SFR_{IR} are derived in a manner presented in Umehata et al. (2018) assuming a Chabrier IMF.

The 860 μm flux densities of the seven components were measured using CASA/IMFIT using the 0.8'' and 1.0'' images as summarized in Table 1. Following Geach et al. (2016), we also measured the total flux density of the 860 μm signal above the 3σ level for the complex, including six galaxies (except for ALMA4) and the Bridge (Table 1). The sum of the individual galaxies and bridge is consistent with the measurement for the whole complex, which suggests that the eight components account for most of the 860 μm flux density. Band 8 and Band 3 photometry are also summarized in Table 1. Two [O III] emitters at $z \approx 3.1$, c1, and c2 (Geach et al. 2016; Li et al. 2021) are not individually detected in dust continuum.

The integrated flux of all components is $S_{860} = 2.66 \pm 0.11$ mJy in the 1.4'' map (Table 2). This value is $\sim 40\%$ larger than the previously reported flux, $S_{860} = 1.86 \pm 0.06$ mJy (Geach et al. 2016). Newly identified relatively extended and/or faint components account for the increase. The updated ALMA-based flux is found to fall in the range of deboosted Submillimetre Common-User Bolometer Array 2 (SCUBA2) measurements ($S_{850} = 3.6 \pm 1.2$ mJy, Geach et al. 2017). We note that it remains unclear whether or not all of the emission observed by the single-dish telescope is completely recovered by ALMA or not, as the remaining uncertainty (0.7 ± 1.2 mJy) indicates.

4. [CII] and CO Emissions in LAB1

4.1. Overview

As shown in Figure 2, the [C II] emission is widely distributed across LAB1 over an area of $d \simeq 100$ kpc, highlighting complex morphology in three-dimensional space. All

seven components identified in the dust continuum are associated with corresponding [C II] emission, confirming that the dust continuum detected within LAB1 is also at $z \approx 3.10$. The picture of the [C II] line has been significantly updated compared to our pilot survey. Umehata et al. (2017a) detected the line only for ALMA3. The deeper observations now confirm that the previous observations also covered the frequency range containing [C II] emission, even though the lower sensitivity prevented actual detection.

To illustrate the overall trend of the [C II] emission projected to a two-dimensional space, we also created a suite of moment maps. For this purpose, we made a *rendered* cube using the naturally weighted, 0.8'' cube. First, voxels that had emission above the 2σ level, measured for each channel before primary beam correction, was extracted from the cube. Second, among them, if a voxel connects to another extracted voxel in velocity space, the voxel was considered to have emission and left in the box. If not, the voxel was masked. Finally, a primary beam correction was applied for each channel. This process allows us to effectively extract extended emission from the data cube, suppressing the influence of noise.

Using the rendered cube, the integrated emission map, the flux-weighted velocity map, and the flux-weighted velocity dispersion map were calculated using CASA/IMMOMENTS task. As shown in Figure 2, the extracted [C II] emission is generally cospatial with dust continuum components. The most dominant five sources (ALMA1–ALMA5) are composed of three groups (ALMA1+2+5, ALMA3, and ALMA4). The remaining two sources are associated with ALMA1+2+5. The velocity map suggests that the emission has complicated velocity structure in a relatively narrow range of flux-weighted velocity (about

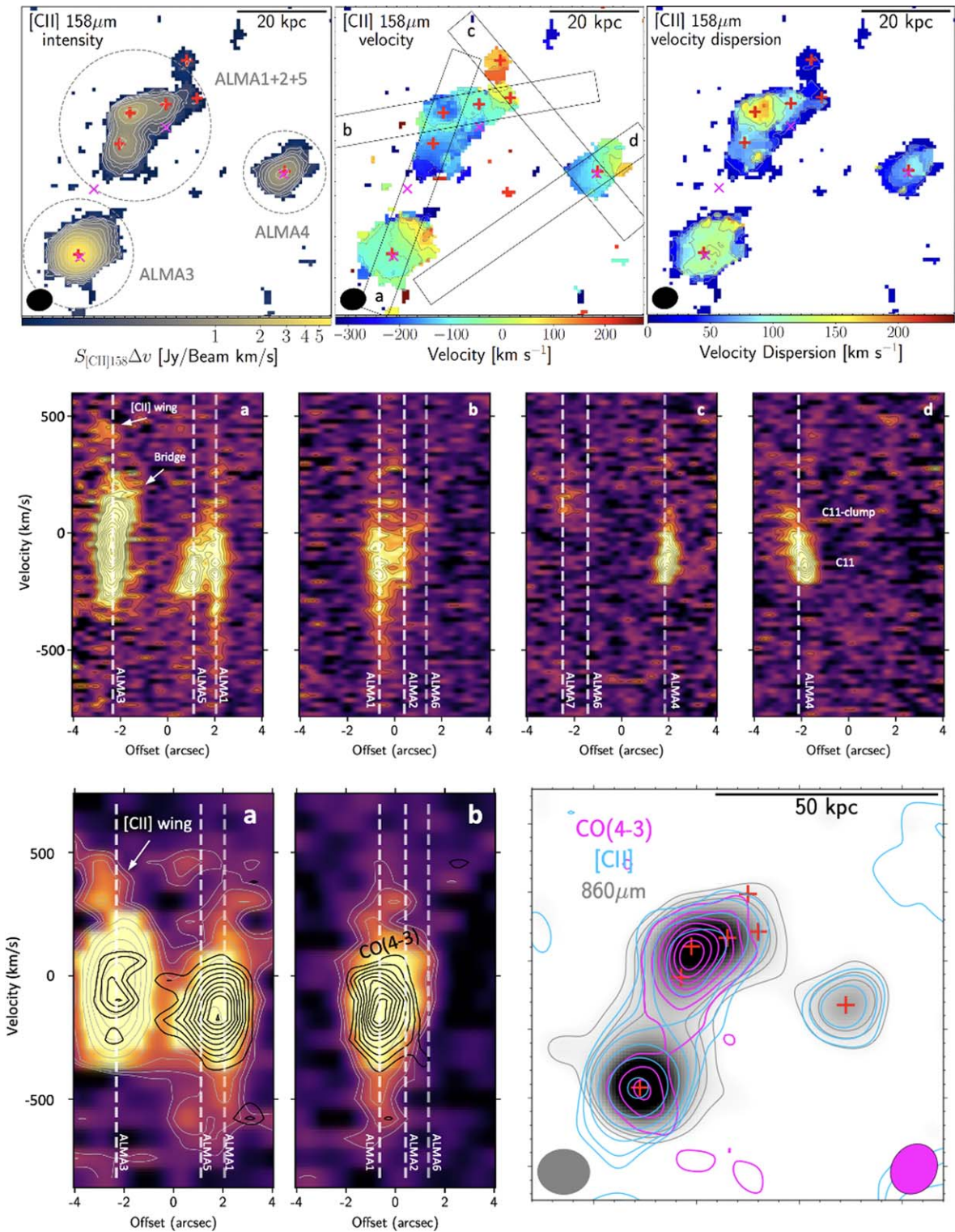


Figure 2. Top row panels show moment maps generated using a *rendered* cube (see Section 4.1 for more details) are displayed to show overall trends of [C II] emission in LAB1. The positions of dust continuum sources and [O III] emitters are shown. Contours are $S_{\text{[C II]}158\mu\text{m}}\Delta v = 0.1 \times [1.5, 1.5^2, \dots, 1.5^{11}] \text{ Jy beam}^{-1} \text{ km s}^{-1}$, in steps of 50 and 25 km s^{-1} relative to $z = 3.100$, from left to right, respectively. The middle row of panels show [C II] position–velocity (P–V) diagrams at $0.8''$ along four slits (*a*–*d*). Contours are in steps of $1\sigma_{\text{center}}$ starting at $2\sigma_{\text{center}}$. ALMA4 and ALMA5 show velocity gradient nearly along the slit, which suggests that they have a rotating gas disk. ALMA4 also has a clump-like structure (“C11 clump”). Multiple-merging events are ongoing among ALMA1, ALMA2, ALMA4, and ALMA6. ALMA3 is accompanied by relatively faint and extended emissions, which is the most remarkable at higher velocities (“[C II] wings”). The bottom left two panels show [C II] P–V diagrams at $1.4''$. CO(4–3) emissions are superposed. Contours show $[1.5^3, 1.5^2, \dots] \times \sigma_{\text{center}}$ and $[2, 3, \dots] \times \sigma_{\text{center}}$, respectively. The bottom right panel shows CO(4–3) and [C II] emission superposed on the $860 \mu\text{m}$ map, integrated over the range of -379 to 101 km s^{-1} . CO(4–3) and [C II] contours are $[2, 4, 8, 16, 32, \text{ and } 64] \times \sigma_{\text{center}}$, while $860 \mu\text{m}$ contours stand for $[2, 3, 4, \text{ and } 5] \times \sigma_{\text{center}}$. The kinematics traced by CO(4–3) is similar to that of [C II]. There is no detectable CO(4–3) emission around ALMA4.

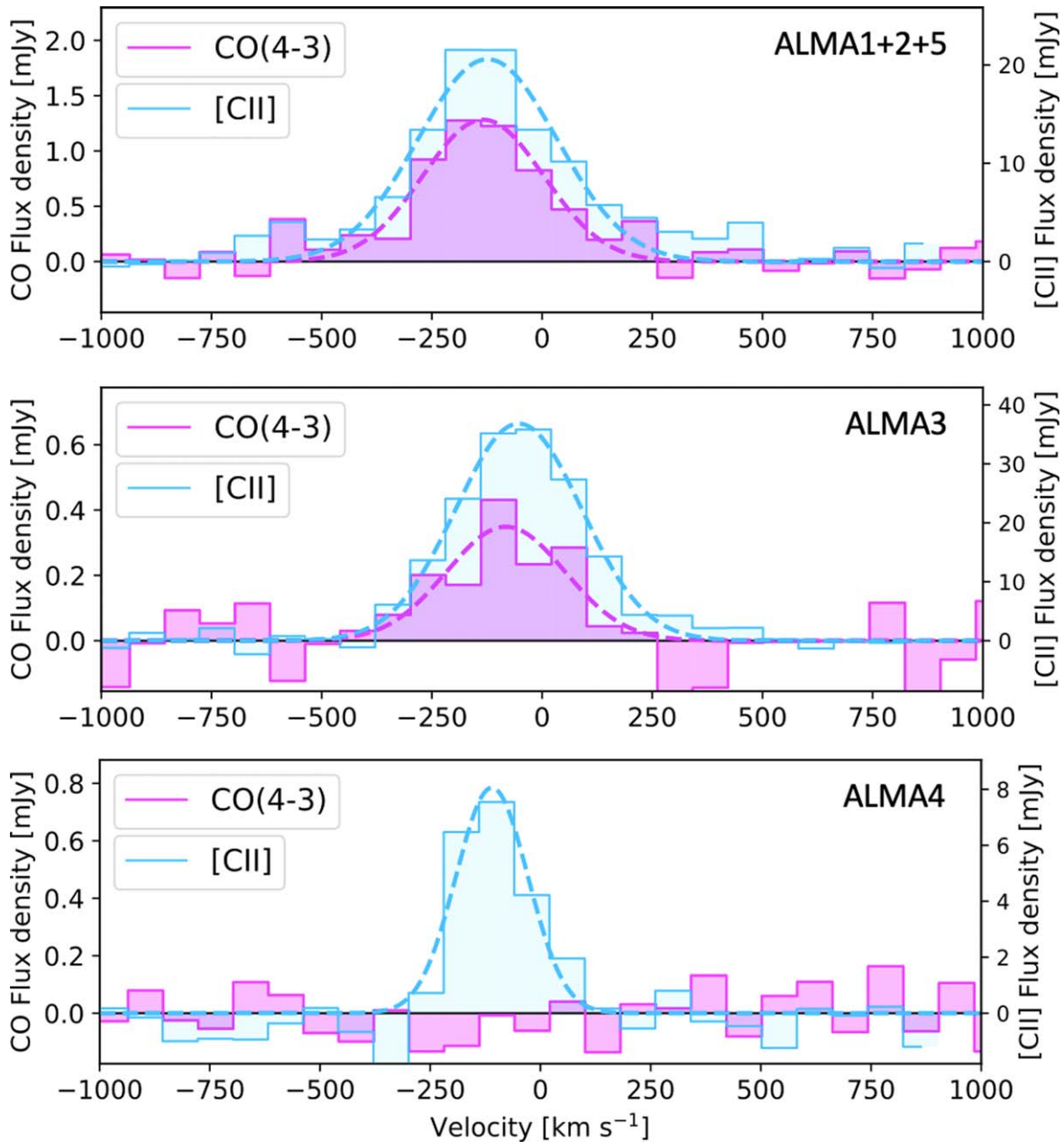


Figure 3. CO(4–3) and [C II] spectra of four regions in LAB1. Velocities are relative to $z = 3.100$. Dashed lines show a Gaussian profile fitted to these emissions. Simultaneous detections of the two emission lines are identified in ALMA1+ALMA2+ALMA5 and ALMA3, while no CO(4–3) line is detected for ALMA4.

-200 to 100 km s^{-1}), while some parts of them, such as ALMA4, show a coherent velocity structure. The velocity dispersion map suggests a variation of (apparent) velocity dispersion (50 – 200 km s^{-1}) among the components, which implies various dynamical states among the cool gas components in LAB1.

The bottom left panel of Figure 2 shows the spatial distributions of CO(4–3), [C II], and $860 \mu\text{m}$ at $1.4''$ resolution. Spectra are shown in Figure 3. The CO(4–3) emission line is identified in ALMA1+2+5 and ALMA3, while ALMA4 has no detected emission. While their spatial distributions are similar on large scales, they are not identical on smaller scales. There is also a wide variety in line ratios, which implies that there are different ISM states among the galaxies in LAB1. Further line diagnostics are beyond the scope of this paper, but

we will present them in an upcoming paper (H. Umehata et al., in preparation).

4.2. Kinematics of the [C II] and CO Emissions

P–V diagrams at $0.8''$ and $1.4''$ resolution are displayed in Figure 2. Each pseudo slit has a width of $0.9''$ to cover the majority of emission along the direction of the velocity gradient, which enables us to discern in more detail the velocity structure and interaction among sources in this complicated system in more detail.

ALMA1+2+5 encompasses ALMA1, ALMA2, ALMA5, as well as ALMA6 and ALMA7. As demonstrated, ALMA1 and ALMA2 are located closely each other (with a projected angular separation $1''$) and overlap in velocity space. This is also the case for ALMA1 and ALMA5. In the $0.8''$ map,

ALMA1 appears to be simultaneously interacting with ALMA2 and ALMA5. The moment map shows that velocity dispersion peaks in the region between ALMA1 and ALMA2, which is also suggestive of turbulent nature there. ALMA6 and ALMA7 show coherent velocity structure, smoothly connecting with ALMA2, which could be additional merging galaxies or tidal tails associated with ALMA2. In Figure 2, slit-a shows a nearly monotonic velocity gradient along the slit at the position of ALMA5 and thus an ordered rotation is indicated. The velocity structure of the CO(4–3) emission is generally consistent with that of [C II]. The emission peak is the closest to ALMA1, while the CO(4–3) profile is also elongated toward ALMA2 and ALMA5.

ALMA3 is the brightest galaxy in [C II] in LAB1, and is also covered by slit-a. There is no significant shift in the centroid position between velocity channels spanning about 400 km s^{-1} around the peak. The Bridge corresponds to a protrusion in a redder part, which is likely to account for the apparent velocity gradient evident in the velocity map. The velocity dispersion of ALMA3 is higher than that of other ALMA sources on galaxy scales (Figure 2), which suggests that turbulence dominates the kinematics in ALMA3. CO(4–3) emission is also identified in ALMA3; it does not show a velocity shift as for [C II]. Slit-a also shows that ALMA3 is accompanied by faint emission with a complicated morphology, including a red [C II] wing. Outflows, tidal tails, or merging satellites could account for the emission.

In the case of ALMA4, there is a nearly monotonic velocity gradient, suggesting a rotating disk. There is a high-velocity clump (C11 clump). Since the C11 clump follows the velocity shift, the system would be kinematically dominated by rotation of C11. However, the velocity dispersion peaks between the dust/stellar peak and the clump, and interaction between the C11 and C11 clump is also implied. ALMA4 has no detectable CO(4–3) emission.

4.3. Radial Profile

Figure 4 shows radial profiles of the dust and gas components at $0.8''$ resolution traced by the $860 \mu\text{m}$ continuum and [C II] emission, respectively. The [C II] emission lines are integrated over a velocity range optimized for each region (see also Figure 5). A combined profile for ALMA1+2+5 is measured, centered at the position of ALMA1. In the case of ALMA3, the Bridge region also contributes in addition to ALMA3 itself. For all cases, both [C II] and dust continuum emission shows similar radial profiles (extending to about 15 kpc). The profiles demonstrate that the gas and dust coexist on a large scale in LAB1. We will discuss the nature of the widely distributed ISM in Section 5.

4.4. Counterparts of ALMA-identified Populations

Observations at optical-to-near-infrared wavelengths provide information on stellar components, tracing rest-frame UV-to-optical emission for galaxies at $z \approx 3.1$. Figure 5 shows an optical image taken with the Hubble Space Telescope (HST; the Space Telescope Imaging Spectrograph (STIS)¹³; Chapman et al. 2004), a K_s -band image obtained with the Subaru Multi-Object InfraRed Camera and Spectrograph (MOIRCS; Uchimoto et al. 2012), and dust continuum observations taken in ALMA Band 8. The [C II] emission is integrated over a velocity

range noted in the figure, and known galaxies are labeled (Chapman et al. 2004; Uchimoto et al. 2012; Kubo et al. 2015, 2016; Geach et al. 2016; Li et al. 2021).

ALMA1, ALMA3, and ALMA4 have significant K_s -band counterparts, which is suggestive of modestly obscured star-forming galaxies. ALMA2, ALMA6, and ALMA7 have possible counterparts (LAB1–4 for ALMA2 and ALMA6 and J1 for ALMA7) with slight offsets,¹⁴ $0.3''$ – $0.6''$. This might be explained by different degrees of dust extinction in a galaxy, a companion, or a tidal component. ALMA5 is blank in the rest-frame UV and optical images, in contrast with its bright [C II] emission. This demonstrates the utility of ALMA to identify populations that would otherwise be missed.

4.5. Measurements of Properties

Since it is not straightforward to isolate line fluxes from the cube in this crowded region, we derive line properties for groups on the basis of $1.4''$ resolution data. The line flux, redshift, and the FWHM of the line profile are calculated from a Gaussian fit to the extracted spectra shown in Figure 3. The velocity-integrated maps (Figure 2) are used to measure sizes of the emissions using CASA/IMFIT. Derived properties are summarized in Table 2. We also extracted [C II] spectra from the $1.0''$ cube at the positions of seven ALMA sources (ALMA1–ALMA7) to measure line properties and derive [C II] line for each (Appendix E).

A suite of other physical properties were also estimated. IR luminosity (L_{IR}) and IR-based SFR (SFR_{IR}) were estimated, scaled $860 \mu\text{m}$ fluxes using spectral energy distribution (SED) templates of SMGs selected from ALMA Observations of Submillimeter Galaxies from the LABOCA Extended Chandra Deep Field South Survey (ALESS) (Danielson et al. 2017) (for more details, see Umehata et al. 2018). As summarized in Table 2, ALMA1+2+5, ALMA3, and ALMA4 have SFR_{IR} of ~ 110 , ~ 100 , and $\sim 20 M_{\odot} \text{ yr}^{-1}$, respectively. These estimates, however, are based on single point photometry and thus remain uncertain.

The CO(4–3) line intensities for ALMA1+2+5 and ALMA3 are derived to be $S \Delta v = 0.44 \pm 0.03$, $0.12 \pm 0.02 \text{ Jy km s}^{-1}$, respectively. We can compare these to earlier attempts to observe the CO(4–3) line from LAB1. Chapman et al. (2004) obtained a marginal detection of the line using the Owens Valley Radio Observatory Millimeter Array and reported a line intensity $S \Delta v < 2.5 \text{ Jy km s}^{-1}$, while Yang et al. (2012) reported a 3σ upper limit $S \Delta v < 0.62 \text{ Jy km s}^{-1}$ using the Plateau de Bure Interferometer. The ALMA observation, which has a better angular resolution, thus confirms that the CO(4–3) emission had evaded detection due to the insufficient sensitivity of these observations. The CO(4–3) line luminosities were calculated following Solomon & Vanden Bout (2005). To estimate molecular gas mass on the basis of the CO(4–3) line, a brightness temperature ratio $r_{41} = L'_{\text{CO}(4-3)} / L'_{\text{CO}(1--0)}$ and a CO-to- H_2 conversion factor α_{CO} must be assumed. The derived IR luminosity range, $\log(L_{\text{IR}}/L_{\odot}) = 11.3$ – 12.0 , is comparable to, or somewhat lower than, that of the ALMA large project of the ALMA Spectroscopic Survey in the Hubble Ultra Deep Field (ASPECS-LP) sample at $z = 2.0$ – 4.0 ($\log(L_{\text{IR}}/L_{\odot}) = 11.6$ – 12.9 , Boogaard et al. 2020). Hence we adopt the brightness temperature ratio $r_{41} = 0.61 \pm 0.13$, which is derived for the $z > 2$ ASPECS galaxies, and $\alpha_{\text{CO}} = 3.6 M_{\odot} (\text{K km s}^{-1} \text{ pc}^2)^{-1}$,

¹⁴ Positional uncertainties (σ_{pos}) related to the signal-to-noise ratio (S/N) and the synthesized beam size (θ_{beam}) are described as $\sigma_{\text{pos}} \approx \theta_{\text{beam}} / (2 \times \text{S/N})$ (Condon 1997). In the case of $\theta_{\text{beam}} = 0.8''$ and $\text{S/N} = 5$, σ_{pos} is thus $\approx 0.08''$, which is smaller than the measured offsets.

¹³ The image has a pivot wavelength of 5733 \AA .

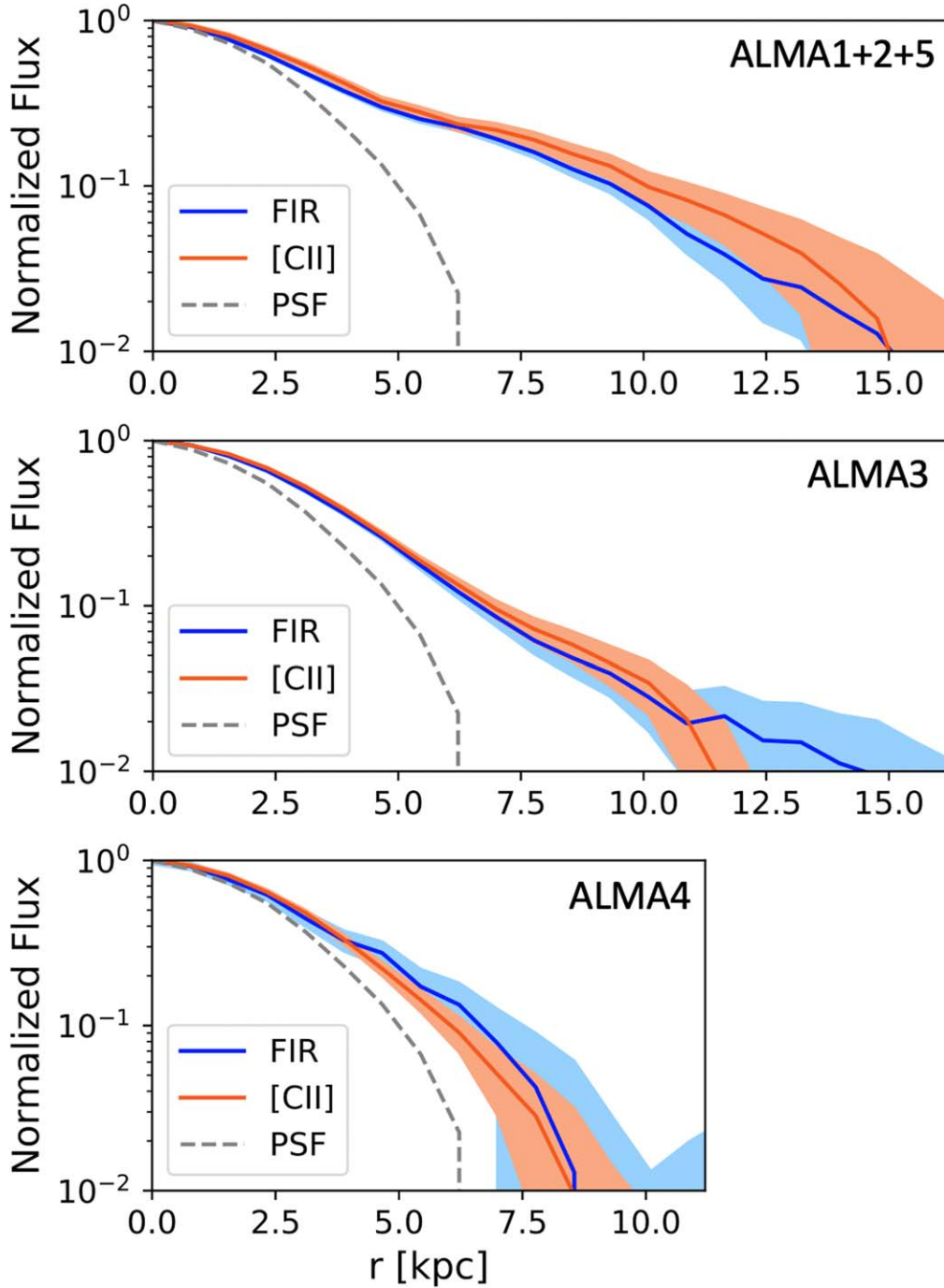


Figure 4. Radial profiles centered at the three bright dusty starbursts in $0.8''$ resolution maps. The $860\ \mu\text{m}$ map is used to show the far-infrared (FIR) profile. Shaded regions show the photometric uncertainties (not including the calibration errors). Radial profiles are generally similar between FIR and [C II] up to about 15 kpc.

which is adopted for the galaxies (Decarli et al. 2020). Estimated molecular gas masses are $M_{\text{gas}} = (6.8 \pm 1.5)$ and $(1.8 \pm 0.5) \times 10^{10} M_{\odot}$ for ALMA1+2+5 and ALMA3, respectively. About 80% of the molecular gas is concentrated in ALMA1+2+5. Measured values are given in Table 2, including an upper limit for ALMA4.

5. Discussion

5.1. The Origin of the [CII] Emission

Both dust and [C II] emission are widely distributed across LAB1, which allows us to investigate the corresponding ISM

properties in a spatially resolved manner. As shown in Figure 6, an IR luminosity density ($\Sigma L_{\text{IR}} [L_{\odot} \text{ kpc}^{-2}]$) map was calculated on the basis of the $1.0''$ $860\ \mu\text{m}$ map as described in Section 4.5. An $L_{\text{[CII]}}/L_{\text{IR}}$ map was then constructed by combining with the $1.0''$ [C II] map. The right hand panel of Figure 6 shows the distribution of $L_{\text{[CII]}}/L_{\text{IR}}$ across LAB1 as a function of ΣL_{IR} . For comparison, the best-fit function and 1σ dispersion derived for local ultraluminous infrared galaxies (ULIRGs) (The Great Observatories All-sky LIRG Survey (GOALS); Díaz-Santos et al. 2017) and a range of resolved galaxies including local sources as well as high-redshift galaxies (Smith et al. 2017) are also displayed.

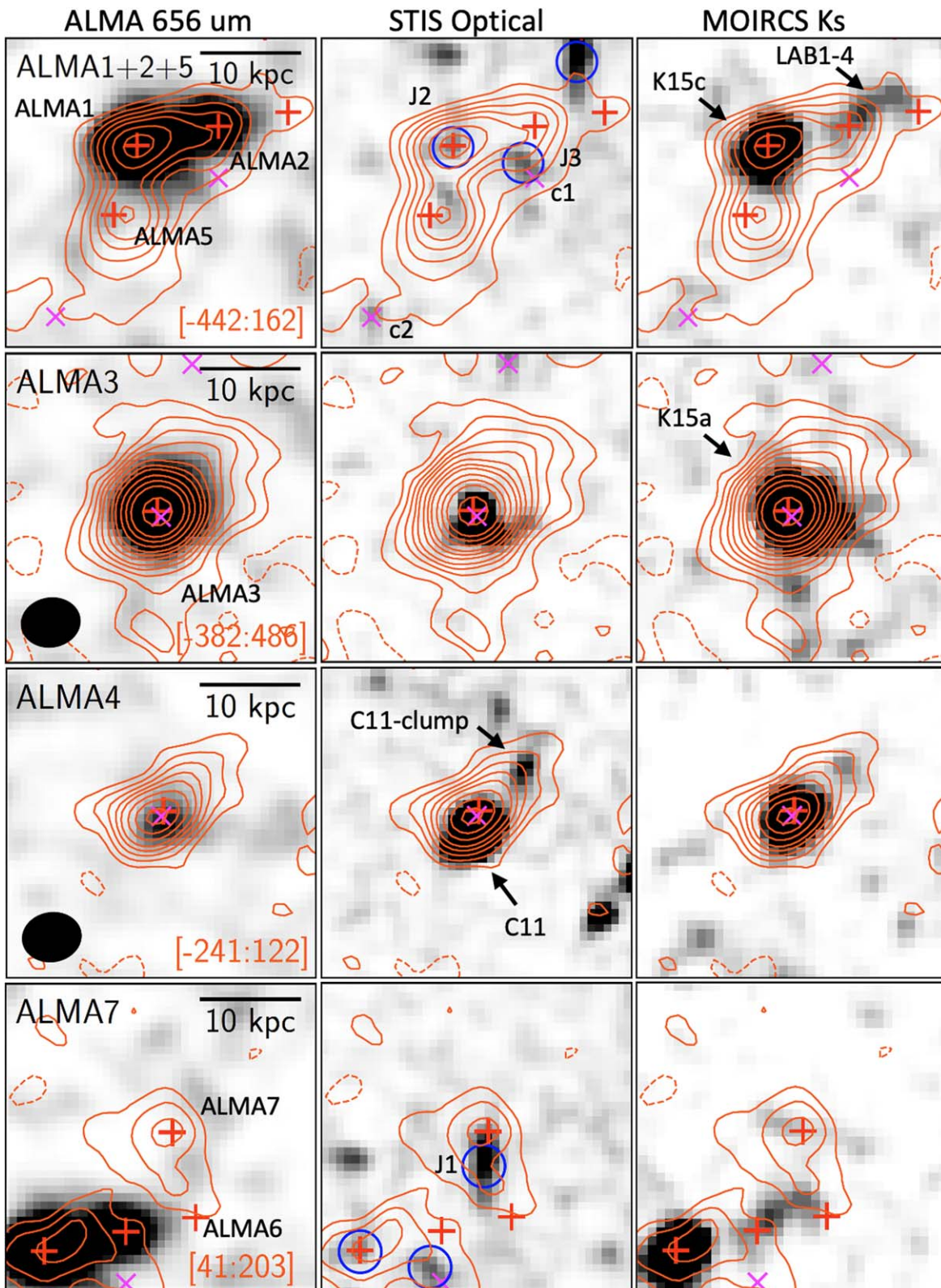


Figure 5. Multiwavelength images of the four [C II]-emitting regions taken with ALMA, HST/STIS Optical (Chapman et al. 2004), and Subaru MOIRCS (Uchimoto et al. 2012). Orange contours show $[-3, 2, 4, 6, 8, 10, 13, 16, 19, 24, 29, 34] \times \sigma_{\text{center}}$ of the integrated [C II] emission. The velocity ranges used are shown in each ALMA panel in units of kilometers per second. Crosses show the positions of dust continuum (red) and [O III] emitters (magenta), while blue circles show faint optical sources identified in Chapman et al. (2004) (J1 also has a VLA counterpart as in Chapman et al. 2004). There is a variety of appearances in the optical and K_s -band images among the ALMA-identified components. ALMA5 has no counterpart and highlights the importance of ALMA observations.

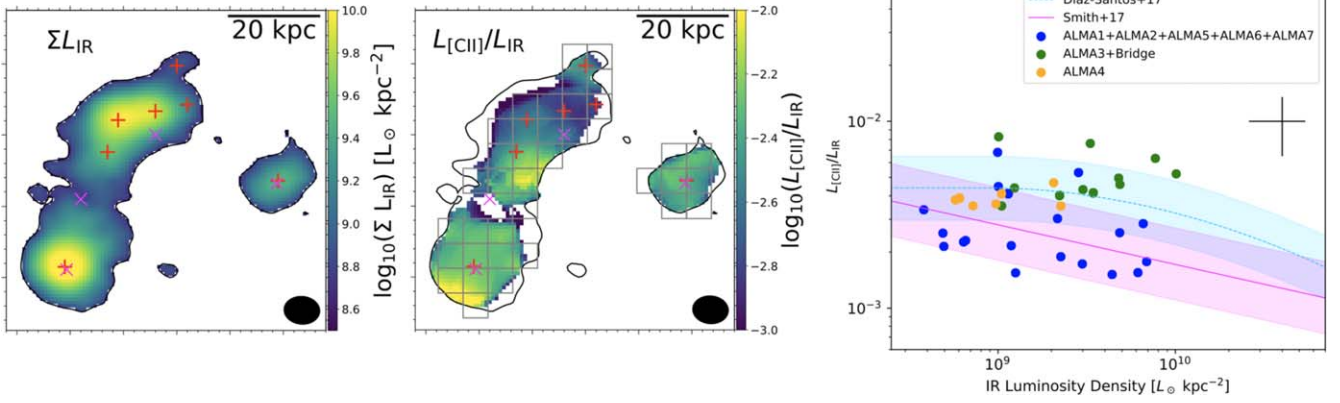


Figure 6. The left panel shows an IR luminosity density map calculated based on the $1.0''$ $860\ \mu\text{m}$ map. The middle panel shows the resolved $L_{[\text{CII}]} / L_{\text{IR}}$ distributions for the areas where both dust and [C II] are detected. The right panel shows $L_{[\text{CII}]} / L_{\text{IR}}$ as a function of IR luminosity density, using the binned values from the middle panel. The [CII]/FIR ratio in LAB1 is broadly consistent with those observed in local galaxies. The [CII]/FIR ratio in LAB1 is broadly consistent with the empirical relations derived by Smith et al. (2017) or the GOALS sample (Díaz-Santos et al. 2017).

It has been established that $L_{[\text{CII}]} / L_{\text{IR}}$ decreases as L_{IR} increases (e.g., Malhotra et al. 1997, 2001; Stacey et al. 2010). This is sometimes called the “[C II] deficit”. It has been reported that $L_{[\text{CII}]} / L_{\text{IR}}$ is more tightly correlated with ΣL_{IR} (or the SFR surface density, ΣSFR) (Smith et al. 2017; Díaz-Santos et al. 2017). Díaz-Santos et al. (2017) propose that the radiation field intensity to gas density ratio, which is related to ΣL_{IR} , is the driver of the [C II] deficit. The new ALMA data enable us to construct a resolved picture for the relation in the low IR density regime at $z = 3.1$ ($\Sigma L_{\text{IR}} \approx 5 \times 10^8 - 10^{10} [L_{\odot} \text{ kpc}^{-2}]$). As shown in Figure 6, the $L_{[\text{CII}]} / L_{\text{IR}}$ ratios in LAB1 are broadly consistent with those observed in local galaxies. This demonstrates that the star-forming galaxies in LAB1 exhibit similar trend to those found in the local universe. Compared with IR-brighter galaxies at high redshift, they may have moderate radiation field strengths. Thus, the relation between $L_{[\text{CII}]} / L_{\text{IR}}$ and ΣL_{IR} shown in Figure 6 supports the idea that the observed, extended ISM, traced by [C II] and the dust continuum, is mainly associated with star formation: as a part of the massive galaxies, a collection of star-forming galaxies that are individually unresolved, or PDRs in outflows. We note that there is currently no evidence to support AGN activity in LAB1 (Geach et al. 2009), although we cannot exclude the possibility that there is a heavily obscured AGN present. Nevertheless, the observed range of $L_{[\text{CII}]} / L_{\text{IR}}$ is higher than the value reported for $z = 1-2$ AGNs ($\log(L_{[\text{CII}]} / L_{\text{IR}}) \sim -3.5$ for AGNs with $10^{13} - 10^{14} L_{\text{IR}}$, Stacey et al. 2010), which is also consistent with a lack of AGN activity.

One plausible explanation for the presence of [C II] and dust continuum beyond the stellar counterparts may be stripping of highly enriched gas from the less strongly bound regions of galaxies from tidal interactions with one another. In addition to interactions among ALMA-identified galaxies, ALMA3 has two nuclei in the HST image, which is suggestive of a late-stage merger (Appendix F). The interactions can strip a significant amount of gas and dust out into the intergroup medium. The presence of undetected companion galaxies with significant dust extinction could also contribute. Future sensitive imaging at optical-to-near-infrared wavelengths, including the James Webb Space Telescope (JWST), will improve our understanding in this regard.

There may be another possible origin for the extended [C II] emission: while [C II] emission is expected to arise primarily from PDRs, it is also observed in other environments, including

shocked gas (e.g., Stacey et al. 1991; Appleton et al. 2013). Appleton et al. (2013) reported the detection of [C II] emission associated with shocked gas in a local interacting galaxy group, Stephan’s quintet. Such regions show higher luminosity ratios, $\log(L_{[\text{CII}]} / L_{\text{IR}}) \approx -1.5$ to -1.0 , which are difficult to explain by star formation alone. The specific environment in LAB1: ongoing mergers and possible association with gas accretion from the CGM/IGM may point to this origin for [C II] emission. However, as discussed above, the measured $L_{[\text{CII}]} / L_{\text{IR}}$ appears to be smaller than expected if shocked gas is dominant mechanism for exciting [C II]. Although, the current estimate has relied on SED templates of bright dusty star-forming galaxies due to the shortage of photometry; this may overestimate the dust temperature for an intergalactic region (or a region in the outskirts of a galaxy) and thus underestimate the $L_{[\text{CII}]} / L_{\text{IR}}$.

In summary, the most plausible scenario is that the observed [C II] emission is principally associated with star formation, although other origins are not excluded.

5.2. Galaxy Assembly via Multiple Merging

ALMA observations reveal that LAB1 is associated with a number of star-forming galaxies. In total, seven galaxies are identified from dust continuum and [C II] together with [O III] $\lambda 5008$ and Ly α lines (Steidel et al. 1998; McLinden et al. 2013; Kubo et al. 2015; Umehata et al. 2017a; Li et al. 2021). There are also two additional [O III] emitters (Geach et al. 2016; Li et al. 2021), and thus to date a total of nine galaxies are confirmed to be located in LAB1 within a projected distance of its center of 40 kpc (here we include all seven components identified at $860\ \mu\text{m}$, while ALMA6 and ALMA7 may be tidal tails of ALMA2 as discussed in Section 4). In addition to the overdensity, interactions among multiple galaxies are suggested from [C II] (as described in Section 4.2). Resolved stellar morphologies are also suggestive of some sort of interaction, showing clumps and tails (Section 4). All together, LAB1 appears to be a site of hierarchical galaxy assembly during a star-forming phase in the early universe. The situation resembles previously reported clusters of bright SMGs, e.g., SSA22-AzTEC14 at $z = 3.1$ (Umehata et al. 2015; Kubo et al. 2016) and the distant red core at $z = 4.0$ (Oteo et al. 2018; Ivison et al. 2020, see also Miller et al. 2018 and Hill et al. 2020), although the components of

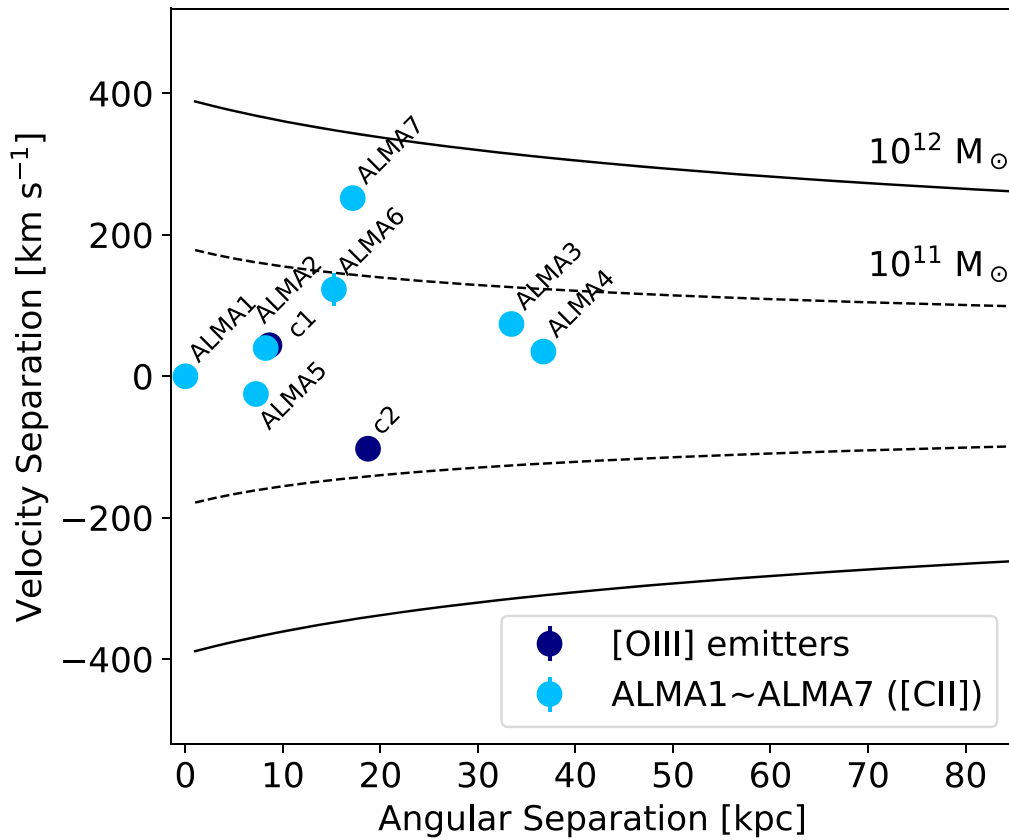


Figure 7. Velocity offsets of the nine sources in LAB1 as a function of projected, physical distance. ALMA1 is assumed to be the center, and navy and light blue points show the [C II]-emitting galaxies and [O III] emitters (Li et al. 2021). Tracks show the escape velocities in the case of an NFW halo with a halo mass ($M_{\text{halo}} = 10^{11} M_{\odot}$ and $10^{12} M_{\odot}$). The galaxies in LAB1 have small velocity offsets, which suggests that they are in the merging phase and not virialized yet.

LAB1 are fainter than those in these systems, providing insights into a poorly understood regime.

In order to investigate the state of LAB1 in the context of galaxy assembly, we use clues from the geometry and dynamics of the member galaxies. Figure 7 shows the line-of-sight velocity offsets for the $z \approx 3.10$ galaxies as a function of projected separation. ALMA1, which is one of the most massive systems in the field and is located close to the centroid of the extended Ly α emission, is adopted as the center. We also plot escape velocities following Kubo et al. (2016). Assuming a Navarro–Frenk–White (NFW) mass profile (Navarro et al. 1997), the escape velocities for a halo of mass $M_{\text{halo}} = 10^{11} M_{\odot}$ and $10^{12} M_{\odot}$ is calculated as a function of separation from the center. We adopted a concentration parameter $c = 4.5$ (Klypin et al. 2011). In order to take the projection effect into account, the physical distance r and the line-of-sight velocity offset v are corrected using an averaged projection factor $2/\pi$ and $1/\sqrt{3}$, respectively (e.g., Jaffé et al. 2015). As shown in Figure 7, the range of velocity separation is relatively small. This is in contrast with another dense group in SSA22 (AzTEC14, Kubo et al. 2016), which has a velocity separation $\approx 1000 \text{ km s}^{-1}$ with a similar angular separation.

In LAB1, the galaxies are distributed within a region expected if they are bounded in a halo with $\lesssim 10^{12} M_{\odot}$. However, this scenario is highly unlikely. Among the $z \approx 3.1$ galaxies, ALMA1, ALMA2, ALMA3, and ALMA4 have K_s -band counterparts (Section 4). The sum of the stellar masses of the four galaxies (i.e., the most massive four members) is estimated to be $M_* \approx 2.2 \times 10^{11} M_{\odot}$ (e.g., Kubo et al. 2016). Hence, the stellar mass–halo mass relation, which is derived

from clustering analysis, suggests a halo with $\sim 10^{13} M_{\odot}$ (e.g., Durkalec et al. 2015). We note that a caveat is the influence of line-of-sight projection on the measured velocity dispersion. While a simple, spherical geometry is assumed in deriving the track of escape velocity in Figure 7, this may not be the case. If we see galaxies in filaments from a viewing angle close to face-on, the apparent velocity offset can be small. Such an effect could account for the observed small velocity range. Considering the data, therefore one possible scenario is that we are witnessing a merging phase of multiple galaxies hosted in multiple halos. If they are merging and not yet virialized, the velocity offsets are expected to be small as observed in LAB1. A multiple-merger phase of star-forming galaxies is expected for a progenitor of a brightest cluster galaxy (BCG) in the nearby universe during hierarchical galaxy assembly in the early universe (e.g., Kubo et al. 2016), and thus an evolutionary connection between BCG formation and LABs may be suggested. This phase tends to occur in halo masses of group size, consistent with our observations.

One issue to be resolved regarding the assembly phase is the deficit of observed low-mass galaxies (e.g., Hatch et al. 2009; Kubo et al. 2016). For instance, Hatch et al. (2009) investigated the stellar-mass distribution of the spiderweb protocluster at $z = 2.2$, and reported that the number of observed galaxies falls for short at $M_* < 10^{9.8} M_{\odot}$, compared to the prediction of semi-analytic models. The existing K -band image of LAB1 allows us to detect relatively unobscured galaxies with $M_* \gtrsim 10^{10.5} M_{\odot}$ at $z \sim 3$ (Kubo et al. 2016). Galaxies newly discovered in [C II] may account for (some of) these galaxies, which are ISM-rich and had been evaded for detection at UV-to-optical

wavelengths due to the extinction. Sensitive census of stellar-mass distributions, which will be possible with the JWST, will allow us to further test such a scenario.

5.3. The Origins of Ly α Emission and Baryon Cycling

The physical nature of LABs is still without a consensus model, with several competing theories. What mechanisms power the enormous and extended Ly α emission is a key issue. The kinematics of the neutral hydrogen traced by Ly α (i.e., inflow and outflow) is also of interest in understanding baryon cycling in a massive halo. LAB1 has been a remarkable target in these contexts since its discovery (e.g., Steidel et al. 2000; Bower et al. 2004; Chapman et al. 2004; Matsuda et al. 2004, 2007; Geach et al. 2005, 2009, 2014, 2016; Mori & Umemura 2006; Weijmans et al. 2010; Hayes et al. 2011; Cen & Zheng 2013; Tamura et al. 2013; Yajima et al. 2013; Hine et al. 2016; Ao et al. 2017; Umehata et al. 2017a; Herenz et al. 2020; Li et al. 2021). Our new ALMA observations provide key information for reassessing LAB1’s nature.

5.3.1. The Central Heating Source and Scattering Scenario

One scenario proposed for the source that powers the Ly α emission is the existence of a central heating source that provides ionizing photons via star formation or AGN (e.g., Steidel et al. 2000; Geach et al. 2009). While AGNs are not confirmed in LAB1 on the basis of X-ray (Geach et al. 2009) or radio observations (Ao et al. 2017), several galaxies that harbor dust-enshrouded star formation have been identified (e.g., Chapman et al. 2004; Geach et al. 2005; Tamura et al. 2013; Geach et al. 2014). Most recently, Geach et al. (2016) identified three dusty sources, corresponding to ALMA1, ALMA2, and ALMA3 in this paper. They showed that Ly α photons escaping from these dusty sources could generate the bright, extended Ly α emission as a result of successive scattering, using a cosmological zoom-in simulation. This is also in line with the detection of a polarized ring nearly centered at the Ly α emission peak (and the position of ALMA1, Hayes et al. 2011). Li et al. (2021) also reported that the observed Ly α /H β ratios are explainable by this scenario, although H β fluxes detected by the authors are generally only from galaxies and there is still room for discussion about the extended Ly α emission.

Here, we start with the *central source(s) and scattering* scenario making use of what we have learned from the ALMA data. One concern in Geach et al. (2016) was the absence of z_{spec} for the two dusty star-forming galaxies located near the center of LAB1. The line detections ([C II], CO(4–3)) from ALMA1+2+5 definitively show that the dusty star-forming galaxies are physically associated with LAB1. On the basis of the new 860 μm map, the integrated 860 μm flux $S_{860} \approx 2.4$ mJy implies $\text{SFR}_{\text{IR}} \approx 210 M_{\odot} \text{yr}^{-1}$ in total.

In addition, the line detections shed light on the faint, relatively *unobscured* star formation. As Matsuda et al. (2007) reported, there is extended emission in the R band within LAB1, which encompasses the ALMA-identified galaxies (Figure 8). The detected [C II] emission is coincident with the emission in the R band and thus likely to be rest-frame UV (centered at around 1550 \AA) emission at $z = 3.1$. We measured the total UV flux in regions enclosed by the 3σ contours in the R band and located within the apertures that enclose the [C II] emission (ALMA1+2+5, ALMA3, and ALMA4), $F_{\nu} \approx 1.3 \times 10^{30} \text{ erg s}^{-1} \text{ Hz}^{-1}$. The inferred SFR from this is $\text{SFR}_{\text{UV}} \approx 90 M_{\odot} \text{yr}^{-1}$ following the

equation $\text{SFR}_{\text{UV}} [M_{\odot} \text{yr}^{-1}] = L_{\nu} \times (1.46 \times 10^{21})^{-1} [\text{W Hz}^{-1}]$ (for the Chabrier IMF, Kennicutt 1998; Salim et al. 2007), and so total UV+IR SFR is $\sim 300 M_{\odot} \text{yr}^{-1}$. The three apertures show roughly equivalent contribution, so that the obscured fractions of total SFR in ALMA1+ALMA2+ALMA5, ALMA3, and ALMA4 are $\sim 80\%$, $\sim 80\%$, and $\sim 40\%$, respectively.

This star-forming activity causes Ly α emission and also provide the ionizing photons ($\nu = 200\text{--}912 \text{ \AA}$) to the surrounding environment (if they escape). Under the assumption of Case-B recombination, the Ly α luminosity generated by the star formation that escape the host galaxy are described as follows:

$$L_{\text{Ly}\alpha} [\text{erg s}^{-1}] = f_{\text{esc, Ly}\alpha} \times 1.89 \times 10^{42} \times \text{SFR} [M_{\odot} \text{yr}^{-1}]. \quad (1)$$

Here, $f_{\text{esc, Ly}\alpha}$ is the escape fraction of Ly α photons. Considering the Ly α luminosity of LAB1, $L_{\text{Ly}\alpha} \approx 10^{44} \text{ erg s}^{-1}$, therefore the star-forming activities can power the Ly α emission if the escape fractions are high enough ($f_{\text{esc, Ly}\alpha} \gtrsim 20\%$).

In this scenario, Ly α photons, produced by star-forming galaxies scatter through circumgalactic H I, producing extended “Ly α halos” (e.g., Steidel et al. 2011). Thus, the gas traced by Ly α emission is expected to associate with outflow motion. As shown in Figure 8, the profiles of Ly α spectra have a common feature at the positions of ALMA components: Ly α has a minimum near the systemic redshift measured by [C II], with a clear redshifted dominant peak and a blueshifted component. This trend is in line with the idea that the observed Ly α emission (mostly) comes from scattering from outflowing gas; outflowing Ly α photons that are backscattered from gas on the far are the most likely to escape obtaining a frequency shift, while absorption by neutral hydrogen and dust is the most significant at the galaxy’s redshift (e.g., Steidel et al. 2011; Erb 2015; Chen et al. 2021). Outflows may also contribute to increasing the covering fraction of neutral hydrogen (Rahmati et al. 2015).

Recently, Li et al. (2021) performed a Monte Carlo radiative transfer modeling for LAB1 using their Ly α cube taken with the Keck Cosmic Web Imager (KCWI). They reproduce the observed Ly α spectra and constrain parameters in their outflow model with multiphase and clumpy hydrogen gas. They reported that a region around ALMA1 has the highest optical depth and H I outflow velocity in the ionized inter-clump medium. ALMA1 is actually at the redshift inferred by their model and the starburst galaxy is likely responsible for these feature, as the authors predict.

Thus, this central heating and scattering scenario is further supported by the newly delivered ALMA data in some respects. The dusty star-forming galaxies uncovered by ALMA undoubtedly play a significant role in powering Ly α emission and ejecting gas, metals, and dust into the surrounding medium.

5.3.2. Additional Sources to Power Ly α Emission

While star formation can apparently explain the Ly α properties of LAB1, it is still unclear whether it is the solo mechanism causing the enormous Ly α emission. While the polarized ring discovered by Hayes et al. (2011) indicates a heating source near the Ly α emission peak, only half of the total SFR comes from the central group. The remaining fractions evidently originate from the outskirts. Furthermore

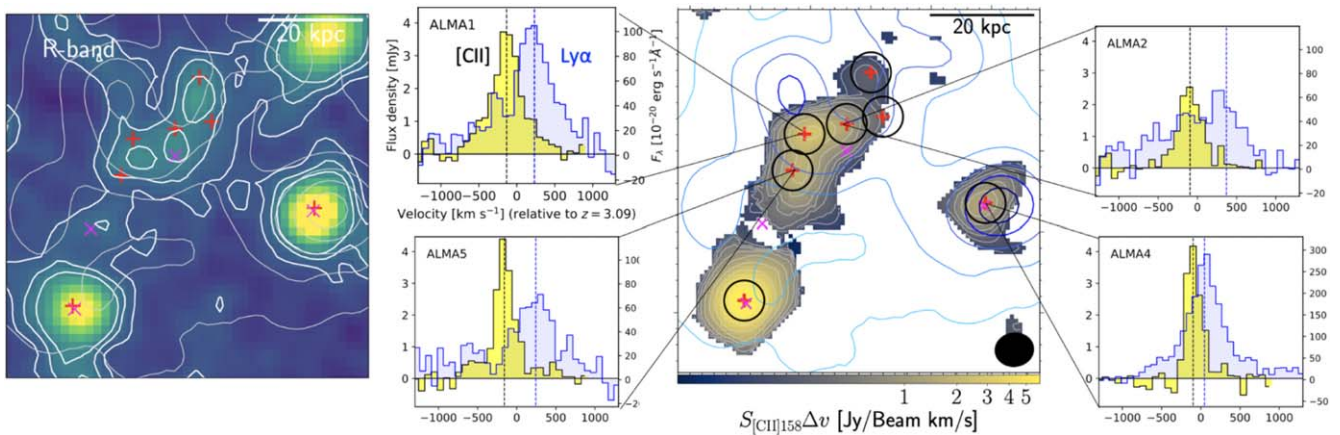


Figure 8. The left panel shows a Subaru/Suprime-Cam R -band image, which traces rest-frame UV ($\approx 1550 \text{ \AA}$) emission at $z \approx 3.1$. Thick contours show $[3, 6, 9] \times \sigma \text{ arcsec}^{-2}$ (Matsuda et al. 2007). Red and magenta crosses shows ALMA sources and [O III]-emitting galaxies as previous figures. The right-hand image shows the rendered, velocity-integrated [C II] intensity map at $1.0''$ resolution with contour levels of $0.1 \times [1.5^2, 1.5^3, \dots] \text{ Jy beam}^{-1} \text{ km s}^{-1}$. Superposed contours with blue colors show the $\text{Ly}\alpha$ emission as in Figure 1. Both [C II] and $\text{Ly}\alpha$ spectra extracted with a $1''$ diameter aperture are also presented for four ALMA components identified at $860 \mu\text{m}$. The $\text{Ly}\alpha$ emission generally has a dominant peak that is redshifted with respect to [C II], which indicates either outflow motion of the H I gas or absorption around the ALMA components.

the obscured fraction of SFR for ALMA1+2+5 and ALMA3 is $\sim 80\%$, and it is uncertain whether these regions would be expected to have relatively high escape fractions of $\text{Ly}\alpha$ photons. There is another clue to strengthen such a caveat. As reported in Umehata et al. (2017b) and Umehata et al. (2018) (see also Umehata et al. 2015), there are a number of SMGs at $z \approx 3.09$ that show higher levels of star-forming activity in the SSA22 protocluster. While a sensitive census of extended $\text{Ly}\alpha$ emission shows that the SMGs ubiquitously reside in $\text{Ly}\alpha$ filaments, the associated $\text{Ly}\alpha$ emission is usually fainter than LABs, in contrast to the activity of associated star formation (Umehata et al. 2019; other examples can be found in Oteo et al. 2018; Li et al. 2019). There is also no evidence favoring exceptionally high escape fractions just for the galaxies in LAB1. These results suggest that the total SFR associated with $\text{Ly}\alpha$ nebulae is not the only key parameter for diagnosing the powering sources of the observed $\text{Ly}\alpha$ emission.

The exceptionally bright and extended $\text{Ly}\alpha$ nature of LAB1 therefore suggests that there is additional mechanism at play, especially in LAB1. A possible path to explain the enhanced $\text{Ly}\alpha$ level in LAB1 is proposed by Yajima et al. (2013). On the basis of a combination of hydrodynamical simulations with three-dimensional radiative transfer calculations, they investigated the environment surrounding a galaxy-galaxy major merger. They successfully produced mock LABs with luminosity of $L_{\text{Ly}\alpha} \sim 10^{42} - 10^{44} \text{ erg s}^{-1}$ and extent of $\sim 50 \text{ kpc}$ at $z \sim 3$. The authors find that both merger-driven intense star formation and cooling radiation induced by strong gravitational interactions contribute to generate $\text{Ly}\alpha$, although the relative fractions are not discussed. While the simulation is only for a binary major merger, they suggest that multiple mergers can generate more spectacular nebulae. As discussed above, LAB1 is found to host ongoing multiple mergers close to the $\text{Ly}\alpha$ emission peak. This is a unique characteristic of LAB1, and suggestive that shocked (collisionally excited) $\text{Ly}\alpha$ may need to be included.

In addition, cold accretion along the filaments has been suggested to be a powering source for years (e.g., Dijkstra & Loeb 2009). Trebitsch et al. (2016) used a radiative hydrodynamics simulation and showed that the observed polarization is explainable with the combination of the *central powering* +

scattering model and $\text{Ly}\alpha$ emission originated from gas during the accretion onto the halo. There is the dominant molecular gas reservoir close to the $\text{Ly}\alpha$ emission peak, which is indicative of gas supply from the cosmic web onto the center of LAB1. Therefore, the ALMA data is not necessarily conflict with the scenario of the cold accretion in this sense.

6. Conclusions

We have carried out deep multiband observations of the giant $\text{Ly}\alpha$ nebulae SSA22-LAB1 at $z = 3.1$ using ALMA. The main conclusions are the following:

1. We performed the most sensitive census to date of dust continuum emission in LAB1 at observed wavelengths of 656 , $860 \mu\text{m}$, and 2.82 mm . The $860 \mu\text{m}$ maps uncover an extended structure of dust emission on a 60 kpc scale, which is decomposed to eight individual components (ALMA1–ALMA7, and the Bridge).
2. [C II] $158 \mu\text{m}$ emission is also widely distributed across LAB1, generally coincident with the $860 \mu\text{m}$ dust continuum. Moment maps and P–V diagrams suggest possible ongoing multiple-merging events involving three dusty galaxies, ALMA1, ALMA2, and ALMA5.
3. Comparison with optical-to-infrared images demonstrates that our previous view of the components of LAB1 has been biased due to heavy dust extinction. A remarkable example is ALMA5, which has no counterpart at near-infrared or optical wavelengths, while a rotating disk structure is suggested by its [C II] emission. The ALMA census sheds light on a number of previously missed LAB1 members.
4. Massive molecular gas reservoirs with $M_{\text{gas}} \approx 10^{11} M_{\odot}$ are uncovered in LAB1 from CO(4–3) emission. We found that the majority of this gas mass is concentrated near the $\text{Ly}\alpha$ peak.
5. The components of LAB1 identified in [C II] and [O III] $\lambda 5008$ show a tight range in redshift, $z = 3.0968 - 3.1016$. LAB1 seems to be in a multiple-merging phase involving a number of galaxies and halos on a group scale, which may be a progenitor of a BCG.

6. The derived (UV+IR) SFRs and profiles of Ly α spectra around dusty galaxies suggest their important role in powering the extended Ly α emission as a heating source. However, it is not clear whether or not star formation in the galaxies is solely responsible. We suggest that cooling radiation induced by strong gravitational interactions may also play a significant role.

We wish to thank the anonymous referee for constructive comments that improved this paper. We acknowledge valuable discussion with Hidenobu Yajima. We thank Scott Chapman and Ken Mawatari for sharing calibrated optical-to-near-infrared images with us. H.U., Y.M. and K.N. acknowledge support from JSPS KAKENHI grant (17KK0098, 20H01953, 19K03937). I.R.S. acknowledges STFC through grant number ST/T000244/1. R.J.I. is funded by the Deutsche Forschungsgemeinschaft (DFG, German Research Foundation) under Germany's Excellence Strategy—EXC-2094 – 390783311. This paper makes use of the following ALMA data: ADS/JAO.ALMA #2013.1.00704.S, #2013.1.00922.S, #2016.1.00485.S, #2016.1.01134.S, #2017.1.01209.S. ALMA is a partnership of ESO (representing its member states), NSF (USA), and NINS (Japan), together with NRC (Canada), MOST and ASIAA (Taiwan), and KASI (Republic of Korea), in cooperation with the Republic of Chile. The Joint ALMA Observatory is operated by ESO, AUI/NRAO, and NAOJ. The National Radio Astronomy Observatory is a facility of the National Science Foundation operated under cooperative agreement by Associated Universities, Inc. Our

data are based on observations collected at the European Organisation for Astronomical Research in the Southern Hemisphere. This research is based on data collected at Subaru Telescope, which is operated by the National Astronomical Observatory of Japan. We are honored and grateful for the opportunity of observing the universe from Maunakea, which is cultural, historical, and natural significance in Hawaii. This research is based on observations made with the NASA/ESA Hubble Space Telescope obtained from the Space Telescope Science Institute, which is operated by the Association of Universities for Research in Astronomy, Inc., under NASA contract NAS 5–26555.

Facilities: ALMA, Subaru, VLT(MUSE), HST(STIS).

Software: astropy (Astropy Collaboration et al. 2013); casa (McMullin et al. 2007); MUSE pipeline (Weilbacher et al. 2016); mpdaf (Piqueras et al. 2017); (Bacon et al. 2016).

Appendix A

The 860 μm Image and Source Decomposition

The 860 μm image was utilized to isolate individual components that were closely located to each other. First the brightest four galaxies identified in the 656 μm image were fitted and subtracted on the image plane using CASA/IMFIT, and the remaining two galaxies were also similarly fitted. Figure 9 shows the original image, best-fit models, and the residual image. As shown, in total seven individual galaxies are identified at 860 μm .

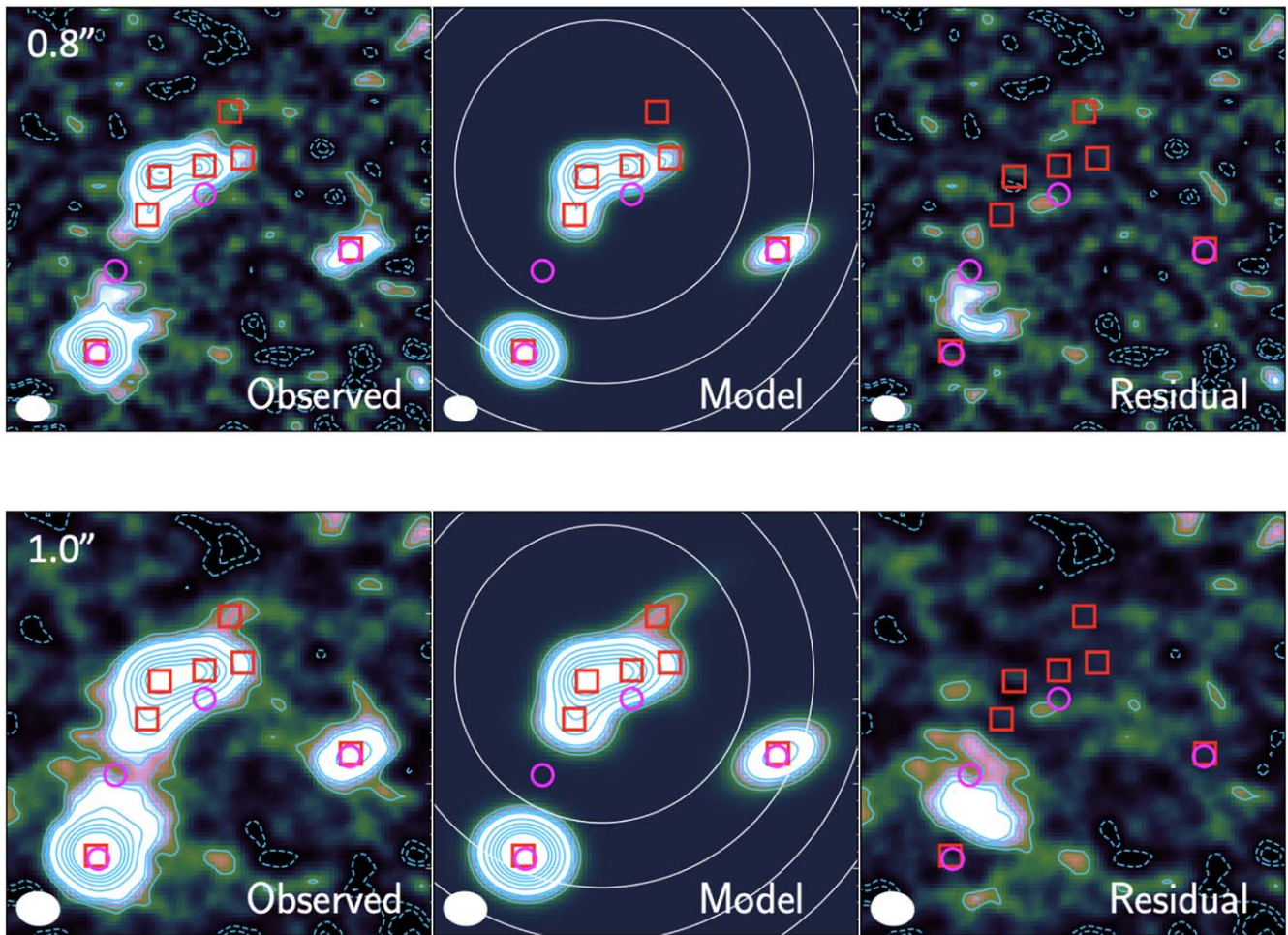


Figure 9. (Left) ALMA 860 μm image at two angular resolutions (0.8'' and 1.0'' as labeled) as shown in the bottom middle panel of Figure 1. Note that the map after primary beam correction is shown here. Contours show $[-3, -2, 2, 3, 4, 5, 10, 15, 20, 25, 30] \times \sigma_{\text{center}}$ emission (σ_{center} shows the rms noise level at the phase center). Red squares show positions of $z = 3.1$ galaxies identified by ALMA, while magenta circles show those of [O III] emitters. (Middle) modeled source profile of six dusty star-forming galaxies at $z = 3.1$. Primary beam responses are also shown using white lines, which correspond to 60%, 70%, 80%, and 90% of the primary beam response. (Right) residual map after subtracted the model images. Extended emission between ALMA3 and ALMA5 is securely detected in both maps.

Appendix B Channel Maps

Figure 10 shows a channel map of [C II] emission in LAB1.

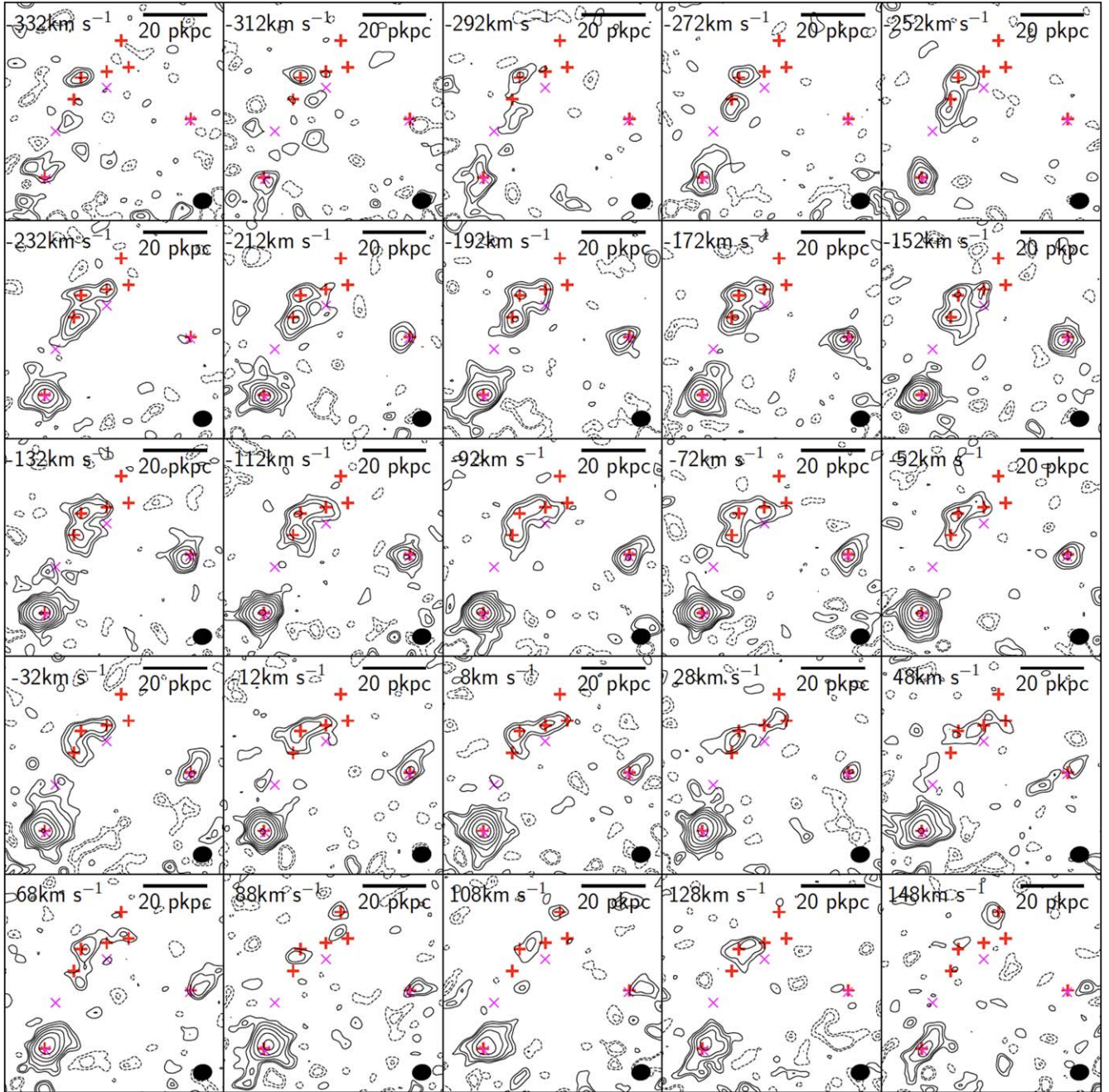


Figure 10. Channel map of [C II] emission in LAB1 in a range of velocity that contains a large fraction of the emission. Each panel is $9'' \times 9''$ in size (corresponding 70×70 kpc at $z \approx 3.1$). Contours show $[-1.5^3, -1.5^2, 1.5^2, 1.5^3, \dots] \times \sigma_{\text{center}}$ of [C II] emission (a fixed value of $\sigma_{\text{center}} = 0.50 \mu\text{Jy}$ is adopted). Crosses show the positions of $860 \mu\text{m}$ -identified components and [O III] $\lambda 5008$ emitters as in Figure 1. [C II] emission is distributed across the field with a complex morphology. All seven components identified in dust continuum are also detected in [C II] and the emission from dust and [C II] are generally cospatial across the field.

Appendix C [CII] Spectra of Two [OIII] Emitters

Two [O III] emitters were discovered by Geach et al. (2016) and Li et al. (2021). The spectra at the reported positions are

shown in Figure 11. Both are likely to be also associated with [C II] emission, but the blending of the nearby bright [C II] sources, and/or a relatively low S/N, prevent us from isolating their contributions.

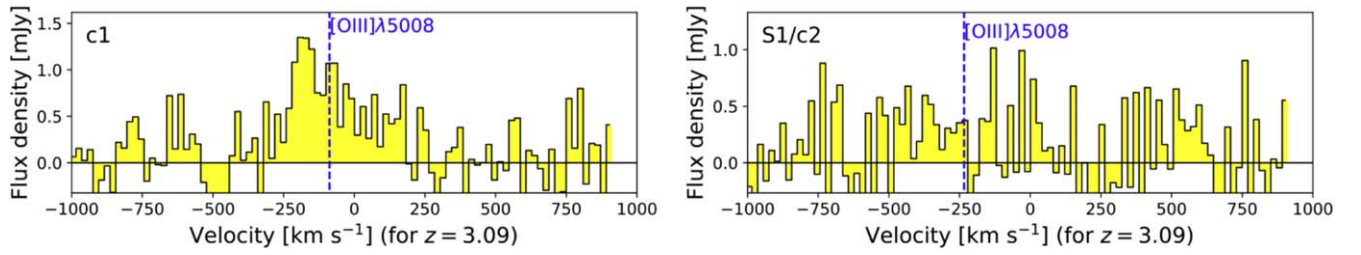


Figure 11. [C II] Spectra of c1 and S1/c2 extracted using a $d = 0.8''$ aperture.

Appendix D

A Galaxy Previously Reported to Be at $z = 3.1$

Kubo et al. (2015) reported that one K_s -band-selected galaxy (K1 or K15b) has a [O III] $\lambda 5008$ emission at $z = 3.1007$ with a moderate significance. However, Li et al. (2020) reported a non-detection of any line from K1 based on their more sensitive observation and hence there is no secure line detection on this source so far. Chapman et al. (2004) argued that the galaxy is likely at a much lower redshift on the basis of U , g , R , I , and K colors. We cannot detect any [C II] (or dust continuum emission) from K1 and so our observations also do not support

the idea that K1 is a member of LAB1. We do not include this source in discussion in this paper. Assuming a 300 km s^{-1} velocity width, a 3σ point source limit of K1 is derived to be $S\Delta v = 0.2 \text{ Jy km s}^{-1}$. For reference, this corresponds to [C II] line luminosity limit $L_{[\text{C II}]} < 7 \times 10^7 L_{\odot}$ in the case of $z = 3.10$.

Appendix E

ISM Properties of Seven ALMA Galaxies in LAB1 at $1.0''$ Resolution

The measured ISM properties of seven ALMA galaxies at $1.0''$ are summarized in Table 3.

Table 3
ISM Properties LAB1 at a 1.0'' Resolution

ID	$z_{\text{[C II]}}$	Δv^a [km s ⁻¹]	$\Delta v_{\text{Ly}\alpha}^b$ [km s ⁻¹]	FWHM [km s ⁻¹]	$S\Delta v$ [Jy km s ⁻¹]	$L_{\text{[C II]}}$ [10 ⁸ L _⊙]	$S_{860 \mu\text{m}}$ [μJy]	L_{IR} [10 ¹¹ L _⊙]
ALMA1	3.0982	-133 ± 10	366 ± 13	482 ± 25	1.75 ± 0.08	6.1 ± 0.3	296 ± 6	2.5 ± 0.8
ALMA2	3.0987	-93 ± 8	464 ± 12	359 ± 21	0.94 ± 0.05	3.3 ± 0.2	224 ± 6	1.9 ± 0.6
ALMA3	3.0992	-59 ± 3	493 ± 32	303 ± 7	5.14 ± 0.11	17.9 ± 0.4	407 ± 8	3.4 ± 1.0
ALMA4	3.0986	-98 ± 6	155 ± 7	220 ± 16	0.99 ± 0.06	3.5 ± 0.2	93 ± 8	0.8 ± 0.2
ALMA5	3.0978	-158 ± 7	402 ± 10	274 ± 18	1.21 ± 0.07	4.2 ± 0.2	127 ± 6	1.1 ± 0.3
ALMA6	3.0999	-10 ± 21	286 ± 24	241 ± 51	0.23 ± 0.04	0.8 ± 0.1	57 ± 6	0.5 ± 0.2
ALMA7	3.1016	119 ± 11	146 ± 14	164 ± 27	0.21 ± 0.03	0.7 ± 0.1	24 ± 7	0.2 ± 0.1

Notes. Line properties are measured through a Gaussian fit to the spectra with a $d = 1''$ aperture (Figure 8). Continuum fluxes are also measured using the same apertures and IR fluxes are calculated using a set of SED templates (Umehata et al. 2017b).

^a [C II] velocity relative to $z = 3.100$.

^b A red peak of Ly α velocity relative to [C II] velocity.

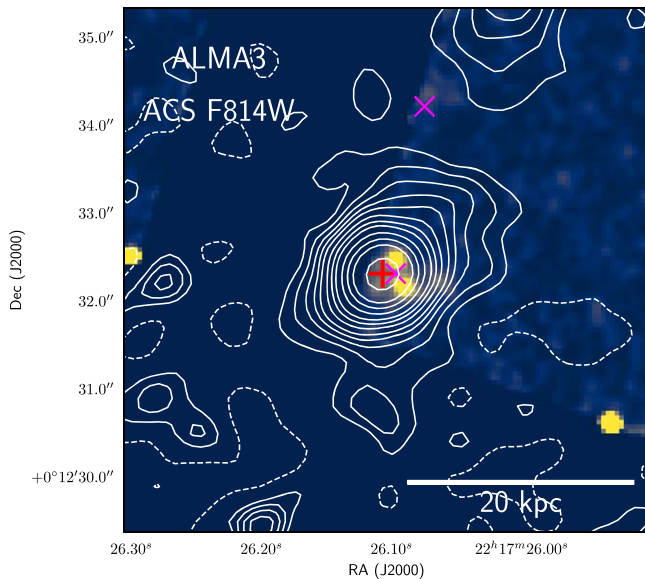


Figure 12. An ALMA3 image taken with HST/ACS using the F814W filter. Contours and markers show [C II] emission and galaxy positions as in Figure 5. ALMA3 is found to have two nuclei or clumps in the band, which is suggestive of a galaxy–galaxy merger–merger.

Appendix F

Advanced Camera for Survey (ACS) Image of ALMA3

A HST image taken with the ACS, with the F814W filter covers LAB1, while LAB1 is located in the edge region of the map. As shown in Figure 12, ALMA3 is found to have two major components at the core. This indicates a merger, while other scenarios like a dusty lane are not excluded.

ORCID iDs

Hideki Umehata <https://orcid.org/0000-0003-1937-0573>
 Ian Smail <https://orcid.org/0000-0003-3037-257X>
 Charles C. Steidel <https://orcid.org/0000-0002-4834-7260>
 Matthew Hayes <https://orcid.org/0000-0001-8587-218X>
 Douglas Scott <https://orcid.org/0000-0002-6878-9840>
 A. M. Swinbank <https://orcid.org/0000-0003-1192-5837>
 R. J. Ivison <https://orcid.org/0000-0001-5118-1313>
 Mariko Kubo <https://orcid.org/0000-0002-7598-5292>
 Kouichiro Nakanishi <https://orcid.org/0000-0002-6939-0372>
 Yuichi Matsuda <https://orcid.org/0000-0003-1747-2891>

Yoichi Tamura <https://orcid.org/0000-0003-4807-8117>

References

- Ao, Y., Matsuda, Y., Henkel, C., et al. 2017, *ApJ*, **850**, 178
 Appleton, P. N., Guillard, P., Boulanger, F., et al. 2013, *ApJ*, **777**, 66
 Astropy Collaboration, Robitaille, T. P., Tollerud, E. J., et al. 2013, *A&A*, **558**, A33
 Bacon, R., Accardo, M., Adjali, L., et al. 2010, *Proc. SPIE*, **7735**, 773508
 Bacon, R., Piqueras, L., Conseil, S., Richard, J., & Shepherd, M. 2016, MPDAF: MUSE Python Data Analysis Framework, ascl:1611.003
 Boogaard, L. A., van der Werf, P., Weiss, A., et al. 2020, *ApJ*, **902**, 109
 Bower, R. G., Morris, S. L., Bacon, R., et al. 2004, *MNRAS*, **351**, 63
 Cai, Z., Fan, X., Yang, Y., et al. 2017, *ApJ*, **837**, 71
 Cantalupo, S., Arrigoni-Battaia, F., Prochaska, J. X., et al. 2014, *Natur*, **506**, 63
 Cen, R., & Zheng, Z. 2013, *ApJ*, **775**, 112
 Chapman, S. C., Lewis, G. F., Scott, D., et al. 2001, *ApJL*, **548**, L17
 Chapman, S. C., Scott, D., Windhorst, R. A., et al. 2004, *ApJ*, **606**, 85
 Chen, M. C., Chen, H.-W., Gronke, M., Rauch, M., & Broadhurst, T. 2021, *MNRAS*, **504**, 2629
 Ciddor, P. E. 1996, *ApOpt*, **35**, 1566
 Condon, J. J. 1997, *PASP*, **109**, 166
 Danielson, A. L. R., Swinbank, A. M., Smail, I., et al. 2017, *ApJ*, **840**, 78
 Decarli, R., Aravena, M., Boogaard, L., et al. 2020, *ApJ*, **902**, 110
 Dey, A., Bian, C., Soifer, B. T., et al. 2005, *ApJ*, **629**, 654
 Diaz-Santos, T., Armus, L., Charmandaris, V., et al. 2017, *ApJ*, **846**, 32
 Dijkstra, M., & Loeb, A. 2009, *MNRAS*, **400**, 1109
 Durkalec, A., Le Fèvre, O., de la Torre, S., et al. 2015, *A&A*, **576**, L7
 Erb, D. K. 2015, *Natur*, **523**, 169
 Faucher-Giguère, C.-A., Lidz, A., Zaldarriaga, M., & Hernquist, L. 2009, *ApJ*, **703**, 1416
 Francis, P. J., Woodgate, B. E., Warren, S. J., et al. 1996, *ApJ*, **457**, 490
 Geach, J. E., Alexander, D. M., Lehmer, B. D., et al. 2009, *ApJ*, **700**, 1
 Geach, J. E., Bower, R. G., Alexander, D. M., et al. 2014, *ApJ*, **793**, 22
 Geach, J. E., Dunlop, J. S., Halpern, M., et al. 2017, *MNRAS*, **465**, 1789
 Geach, J. E., Matsuda, Y., Smail, I., et al. 2005, *MNRAS*, **363**, 1398
 Geach, J. E., Narayanan, D., Matsuda, Y., et al. 2016, *ApJ*, **832**, 37
 Hatch, N. A., Overzier, R. A., Kurk, J. D., et al. 2009, *MNRAS*, **395**, 114
 Hayashino, T., Matsuda, Y., Tamura, H., et al. 2004, *AJ*, **128**, 2073
 Hayes, M., Scarlata, C., & Siana, B. 2011, *Natur*, **476**, 304
 Hennawi, J. F., Prochaska, J. X., Cantalupo, S., et al. 2015, *Sci*, **348**, 779
 Herenz, E. C., Hayes, M., & Scarlata, C. 2020, *A&A*, **642**, A55
 Hill, R., Chapman, S., Scott, D., et al. 2020, *MNRAS*, **495**, 3124
 Hine, N. K., Geach, J. E., Matsuda, Y., et al. 2016, *MNRAS*, **460**, 4075
 Israel, F. P., Maloney, P. R., Geis, N., et al. 1996, *ApJ*, **465**, 738
 Ivison, R. J., Biggs, A. D., Bremer, M., Arumugam, V., & Dunne, L. 2020, *MNRAS*, **496**, 4358
 Ivison, R. J., Smail, I., Le Borgne, J. F., et al. 1998, *MNRAS*, **298**, 583
 Jaffé, Y. L., Smith, R., Candlish, G. N., et al. 2015, *MNRAS*, **448**, 1715
 Keel, W. C., Cohen, S. H., Windhorst, R. A., & Waddington, I. 1999, *AJ*, **118**, 2547
 Kennicutt, R. C. J. 1998, *ARA&A*, **36**, 189
 Kikuta, S., Matsuda, Y., Cen, R., et al. 2019, *PASJ*, **71**, L2
 Klypin, A. A., Trujillo-Gomez, S., & Primack, J. 2011, *ApJ*, **740**, 102
 Kubo, M., Yamada, T., Ichikawa, T., et al. 2015, *ApJ*, **799**, 38

- Kubo, M., Yamada, T., Ichikawa, T., et al. 2016, *MNRAS*, **455**, 3333
- Li, Q., Cai, Z., Prochaska, J. X., et al. 2019, *ApJ*, **875**, 130
- Li, Z., Steidel, C. C., Gronke, M., & Chen, Y. 2020, arXiv:2008.09130
- Li, Z., Steidel, C. C., Gronke, M., & Chen, Y. 2021, *MNRAS*, **502**, 2389
- Malhotra, S., Helou, G., Stacey, G., et al. 1997, *ApJL*, **491**, L27
- Malhotra, S., Kaufman, M. J., Hollenbach, D., et al. 2001, *ApJ*, **561**, 766
- Matsuda, Y., Iono, D., Ohta, K., et al. 2007, *ApJ*, **667**, 667
- Matsuda, Y., Yamada, T., Hayashino, T., et al. 2004, *AJ*, **128**, 569
- Matsuda, Y., Yamada, T., Hayashino, T., et al. 2011, *MNRAS*, **410**, L13
- Matsuda, Y., Yamada, T., Hayashino, T., Yamauchi, R., & Nakamura, Y. 2006, *ApJL*, **640**, L123
- McLinden, E. M., Malhotra, S., Rhoads, J. E., et al. 2013, *ApJ*, **767**, 48
- McMullin, J. P., Waters, B., Schiebel, D., Young, W., & Golap, K. 2007, in ASP Conf. Ser. 376, *Astronomical Data Analysis Software and Systems XVI*, ed. R. A. Shaw, F. Hill, & D. J. Bell (San Francisco, CA: ASP), 127
- Miller, T. B., Chapman, S. C., Aravena, M., et al. 2018, *Natur*, **556**, 469
- Mori, M., & Umemura, M. 2006, *Natur*, **440**, 644
- Navarro, J. F., Frenk, C. S., & White, S. D. M. 1997, *ApJ*, **490**, 493
- Oteo, I., Ivison, R. J., Dunne, L., et al. 2018, *ApJ*, **856**, 72
- Ouchi, M., Ono, Y., Egami, E., et al. 2009, *ApJ*, **696**, 1164
- Piqueras, L., Conseil, S., Shepherd, M., et al. 2017, arXiv:1710.03554
- Rahmati, A., Schaye, J., Bower, R. G., et al. 2015, *MNRAS*, **452**, 2034
- Salim, S., Rich, R. M., Charlot, S., et al. 2007, *ApJS*, **173**, 267
- Shibuya, T., Ouchi, M., Konno, A., et al. 2018, *PASJ*, **70**, S14
- Smith, J. D. T., Croxall, K., Draine, B., et al. 2017, *ApJ*, **834**, 5
- Solomon, P. M., & Vanden Bout, P. A. 2005, *ARA&A*, **43**, 677
- Stacey, G. J., Geis, N., Genzel, R., et al. 1991, *ApJ*, **373**, 423
- Stacey, G. J., Hailey-Dunsheath, S., Ferkinhoff, C., et al. 2010, *ApJ*, **724**, 957
- Steidel, C. C., Adelberger, K. L., Dickinson, M., et al. 1998, *ApJ*, **492**, 428
- Steidel, C. C., Adelberger, K. L., Shapley, A. E., et al. 2000, *ApJ*, **532**, 170
- Steidel, C. C., Bogosavljević, M., Shapley, A. E., et al. 2011, *ApJ*, **736**, 160
- Swinbank, A. M., Harrison, C. M., Trayford, J., et al. 2017, *MNRAS*, **467**, 3140
- Tamura, Y., Matsuda, Y., Ikarashi, S., et al. 2013, *MNRAS*, **430**, 2768
- Taniguchi, Y., & Shioya, Y. 2000, *ApJL*, **532**, L13
- Trebtsch, M., Verhamme, A., Blaizot, J., & Rosdahl, J. 2016, *A&A*, **593**, A122
- Uchimoto, Y. K., Yamada, T., Kajisawa, M., et al. 2012, *ApJ*, **750**, 116
- Umehata, H., Fumagalli, M., Smail, I., et al. 2019, *Sci*, **366**, 97
- Umehata, H., Hatsukade, B., Smail, I., et al. 2018, *PASJ*, **70**, 65
- Umehata, H., Matsuda, Y., Tamura, Y., et al. 2017a, *ApJL*, **834**, L16
- Umehata, H., Smail, I., Swinbank, A. M., et al. 2020, *A&A*, **640**, L8
- Umehata, H., Tamura, Y., Kohno, K., et al. 2015, *ApJL*, **815**, L8
- Umehata, H., Tamura, Y., Kohno, K., et al. 2017b, *ApJ*, **835**, 98
- Weijmans, A.-M., Bower, R. G., Geach, J. E., et al. 2010, *MNRAS*, **402**, 2245
- Weilbacher, P. M., Streicher, O., & Palsa, R. 2016, MUSE-DRP: MUSE Data Reduction Pipeline, ascl:1610.004
- Yajima, H., Li, Y., & Zhu, Q. 2013, *ApJ*, **773**, 151
- Yang, Y., Decarli, R., Dannerbauer, H., et al. 2012, *ApJ*, **744**, 178
- Yang, Y., Zabludoff, A., Tremonti, C., Eisenstein, D., & Davé, R. 2009, *ApJ*, **693**, 1579